J. Fluid Mech. (2022), *vol*. 941, A49, doi:10.1017/jfm.2022.308

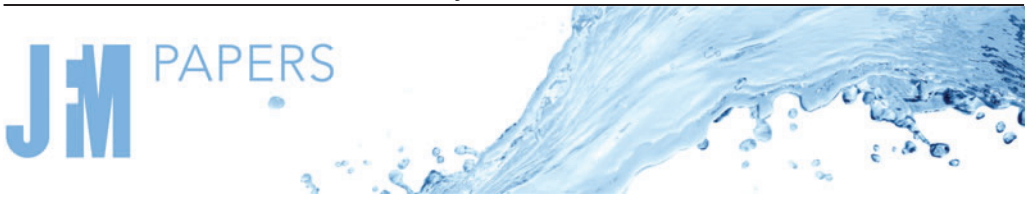

Upscaling of a Cahn–Hilliard Navier–Stokes model with precipitation and dissolution in a thin strip

Lars von Wolff[1],† **and Iuliu Sorin Pop**[2],†

[1]Institute of Applied Analysis and Numerical Simulation, University of Stuttgart, Pfaffenwaldring 57, 70569 Stuttgart, Germany

[2]Faculty of Sciences, Hasselt University, Agoralaan Gebouw D, 3590 Diepenbeek, Belgium

(Received 29 June 2021; revised 10 January 2022; accepted 20 March 2022)

We consider a phase-field model for the incompressible flow of two immiscible fluids. This model extends widespread models for two fluid phases by including a third, solid phase, which can evolve due to e.g. precipitation and dissolution. We consider a simple, two-dimensional geometry of a thin strip, which can still be seen as the representation of a single pore throat in a porous medium. Under moderate assumptions on the Péclet number and the capillary number, we investigate the limit case when the ratio between the width and the length of the strip goes to zero. In this way, and employing transversal averaging, we derive an upscaled model. The result is a multi-scale model consisting of the upscaled equations for the total flux and the ion transport, while the phase-field equation has to be solved in cell problems at the pore scale to determine the position of interfaces. We also investigate the sharp-interface limit of the multi-scale model, in which the phase-field parameter approaches 0. The resulting sharp-interface model consists only of Darcy-scale equations, as the cell problems can be solved explicitly. Notably, we find asymptotic consistency, that is, the upscaling process and the sharp-interface limit commute. We use numerical results to investigate the validity of the upscaling when discontinuities are formed in the upscaled model.

Key words: porous media, multiphase flow

1. Introduction

Multi-phase flow and reactive transport in porous media are encountered in many important fields, including geological CO_2 sequestration, geothermal energy, groundwater

† Email addresses for correspondence: lars.von-wolff@mathematik.uni-stuttgart.de, sorin.pop@uhasselt.be

© The Author(s), 2022. Published by Cambridge University Press. This is an Open Access article, distributed under the terms of the Creative Commons Attribution licence (https://creativecommons.org/licenses/by/4.0/), which permits unrestricted re-use, distribution, and reproduction in any medium, provided the original work is properly cited.

https://doi.org/10.1017/jfm.2022.308 Published online by Cambridge University Press

management, oil recovery and ion exchange in fuel cells. While the modelling of multi-phase flow is itself a challenging task, the examples given before have in common that the solid matrix of the porous medium can change in time due to processes such as precipitation or dissolution, which, in turn influence the flow behaviour.

Another common point of the processes mentioned before is that they take place in a porous medium. In this case, two different length scales are encountered. The first is the pore scale, where each phase (solid, or fluid) can be identified clearly, occupying certain positions in well-defined volumes. The second is the so-called Darcy scale, which is used in most situations of practical relevance, and where averaged quantities are used to describe the behaviour of the system.

Such processes can be modelled at different scales. When formulated at the pore scale, the models are capable of describing the detailed processes accurately. On the other hand, they are defined in a highly complex domain, the union of the pores of in the porous medium, and this makes such models difficult to use for real-life applications. Instead, Darcy-scale models are formulated without taking into account the detailed behaviour of the system at the pore scale, employing constitutive relationships that are stated directly at this larger scale. Therefore, one may say that Darcy-scale models are suited for practical applications, but are missing the accuracy of the pore-scale models. In this context, upscaling is a natural way to derive mathematical models that, on one hand, can be used for practical applications, and, on the other hand, do incorporate accurately the processes taking place at the pore scale. We refer to Dentz *et al.* (2011) for an overview of reactive transport models in porous media.

In detail, we are interested here in the situation where two immiscible fluid phases occupy the pore space of a porous medium. One fluid phase contains ions that can precipitate at the fluid–solid interfaces. This leads to the formation of a precipitate layer at the pore walls, which reduces the space available for the fluid. The reverse process, that is the dissolution of the mineral phase into the fluid phase, is also allowed. In this case, the volume of the precipitate is reduced, while the volume available for flow is increased, and more ions are dissolved in the fluid phase. More precisely, the pore-scale model uses the conservation of mass, momentum and of the dissolved ions in each phase. The challenging aspect here is related to the fact that the spaces occupied by each of the two fluids, as well as by the mineral, can change over time in an *a priori* unknown manner. Therefore, the different phases are separated at the pore scale by free boundaries, which are unknowns in the model. After upscaling, these free boundaries translate into unknown Darcy-scale quantities such as fluid saturation, mineral concentration or the porosity and permeability of the medium. In particular, the latter become time- and space-dependent unknowns, satisfying evolution equations. This is not the case of commonly used Darcy-scale models, where, as mentioned, a given relationship between quantities at the Darcy scale is assumed (e.g. the Cozeny–Kármán relationship).

Different approaches have been proposed when developing mathematical models for applications involving free boundaries at the pore scale. For a simple geometry, which is basically a long, thin strip (in two spatial dimensions) or tube (in three dimensions) the free boundaries can be viewed as functions of one or two variables. In this sense we mention van Noorden (2009*a*) for a model describing precipitation and dissolution but for one fluid phase, which has been extended in Agosti *et al.* (2016), Bringedal *et al.* (2015), Kumar, van Noorden & Pop (2011) and Kumar, Wheeler & Wick (2013) to incorporate non-isothermal or mechanical effects, or in different flow and reaction kinetics regimes but still for the saturated, single-phase flow, and Mikelić & Paoli (2000); Mikelić (2009); Picchi & Battiato (2018); Sharmin, Bringedal & Pop (2020); Lunowa, Bringedal & Pop (2021) for unsaturated single-phase flow or two-phase flow models.

https://doi.org/10.1017/jfm.2022.308 Published online by Cambridge University Press

For more complex geometries, level sets can be employed to describe the evolution of the free boundaries. In this respect we refer to van Noorden (2009*b*), as well as to Bringedal *et al.* (2016); Schulz *et al.* (2017); Schulz (2019), all considering models for precipitation and dissolution in a water-saturated porous medium.

When applying any of both approaches mentioned before, one has to deal with (freely) moving interfaces. This makes not only the mathematical analysis, but also the development of efficient numerical scheme, a challenging task. Alternatively, one can use phase fields to approximate the interfaces between phases by diffuse transition zones with small positive width. The phase fields are smooth approximations of the indicator function of each phase. The evolution of the phase fields is usually derived as the gradient flow to a free energy and, in the limit case when passing the diffuse-interface parameter, one should recover the original, free boundary model.

Commonly used phase-field models involve either the Allen–Cahn equation (Allen & Cahn 1979) or the Cahn–Hilliard equation (Cahn & Hilliard 1958). While the Allen–Cahn equation is of second order and ensures that the phase-field indicators remain essentially bonded by zero and one, it is not conservative. Therefore, we focus here on the Cahn–Hilliard equation, which is of fourth order but conservative for the phase-field indicators.

Models coupling the Cahn–Hilliard equations and the incompressible Navier–Stokes equations have been developed for two fluid phases (Abels, Garcke & Grün 2012), three fluid phases (Boyer & Lapuerta 2006; Boyer *et al.* 2010) and more than three fluid phases (Boyer & Minjeaud 2014; Dunbar, Lam & Stinner 2019). For the description of fluid–solid interfaces, the Navier–Stokes equations can be solved in the fluid volume fraction and a velocity of zero is assigned to the solid phase (Beckermann *et al.* 1999; Sun & Beckermann 2004). Phase-field models are also used in Baňas & Mahato (2017), Bunoiu *et al.* (2020), Daly & Roose (2015), Metzger & Knabner (2021), Schmuck *et al.* (2012) and Schmuck *et al.* (2013) as pore-scale models for two-phase flows in porous media, and further Darcy-scale models are derived. Kinetic reactions at phase boundaries have been introduced in van Noorden & Eck (2011) and Redeker, Rohde & Sorin Pop (2016). The pore-scale model in Redeker *et al.* (2016) includes two immiscible fluid phases and a mineral one, but the fluid phases only move due to curvature effects. Also, the corresponding Darcy-scale model is derived by homogenization techniques. More recently, phase-field models that couple precipitation and dissolution with fluid flow have been developed in Bringedal, von Wolff & Pop (2020) (for one fluid phase, and for which the Darcy-scale model is derived), and Rohde & von Wolff (2021) for a two-phase flow.

The starting point in this work is the Cahn–Hilliard–Navier–Stokes model developed in Rohde & von Wolff (2021), which describes the processes at the pore scale. The aim is to derive an upscaled model corresponding to the Darcy scale. We consider the simplified geometry of a thin strip, and assume that the ratio of the width of the strip and its width is small. We employ asymptotic expansion methods that use this ratio as expansion parameter, and derive upscaled equations for transversally averaged quantities. In this respect, we follow the ideas in Bringedal *et al.* (2015), Kumar *et al.* (2011) and van Noorden (2009*a*) for one-phase flow including precipitation and dissolution effects at the pore walls, and Mikelić & Paoli (2000); Mikelić (2009); Sharmin *et al.* (2020) and Lunowa *et al.* (2021) for two-phase flow, all considering a thin strip or tube. Observe that the pore-scale models in these works mentioned above involve free boundaries. Instead, for the phase-field pore-scale model in Bringedal *et al.* (2020) describing the flow of one fluid phase but including precipitation and dissolution, a Darcy-scale model is also derived for a thin strip by transversal averaging, in comparison with the one obtained by homogenization in more general situations.

https://doi.org/10.1017/jfm.2022.308 Published online by Cambridge University Press

We recall that the geometry considered here is simplified, a long and thin pore. In this case, asymptotic expansion methods and transversal averaging are sufficient to derive the Darcy-scale models. For completeness, we mention that, for general geometries, different techniques may be needed. Restricted to processes involving free boundaries at the pore scale, and particularly to two-phase flows, with or without mineral precipitation or dissolution, both homogenization and volume averaging methods are suited for deriving Darcy-scale models. Homogenization is used in Bringedal *et al.* (2016), van Noorden (2009*b*), Schulz *et al.* (2017) and Schulz (2019) for models based on level sets, and in Bunoiu *et al.* (2020), Bringedal *et al.* (2020), Redeker *et al.* (2016) and Schmuck *et al.* (2013) for phase-field approaches. Alternatively, volume averaging methods are used e.g. in Bahar *et al.* (2016), Quintard & Whitaker (1988), Quintard & Whitaker (1994), Whitaker (1986) and Tartakovsky *et al.* (2007) to derive Darcy-scale models for two-phase flow or reactive transport in porous media. Finally, we also mention that Darcy-scale models for problems of the type discussed here can be obtained by the thermodynamically constrained averaging theory, as done in Gray & Miller (2005), Jackson *et al.* (2012) and Rybak, Gray & Miller (2015).

The main contributions here are threefold. First, starting from a pore-scale model, asymptotic expansion arguments are employed to derive a two-scale model for the two-phase flow in a porous medium, in which the dissolution and precipitation effects are taken explicitly into account. Compared with commonly used Darcy-scale models, instead of postulating relationships between the Darcy-scale quantities such as porosity and permeability, these are obtained here by solving (pore-scale) cell problems. Also, the situation considered here is more complex than in previous publications with a similar focus, as the flow of both fluids is governed by the Navier–Stokes equations, and the flow is coupled to dissolution and precipitation. Second, it is shown that, when letting the Cahn number approach zero, the limit of the two-scale phase-field model is an upscaled sharp-interface model. Finally, it is shown that the two processes, the upscaling and the sharp-interface limit, do commute. In other words, when starting with a diffuse-interface model at the pore scale, the order in which the Cahn number and the aspect ratio of the pore approach zero makes no difference, the result being in either case the upscaled counterpart of the sharp-interface model.

This paper is organized as follows. First, in § 2 a sharp-interface model for two fluid phases and one solid phase (including precipitation and dissolution) is presented. This model is approximated by the phase-field model proposed by Rohde & von Wolff (2021), which is discussed briefly in § 3. After bringing the phase-field model to a non-dimensional form in § 4, in § 5 we derive its upscaled counterpart by considering a thin strip geometry. The upscaled model still uses phase-field variables to locate the diffuse interfaces. In § 6 we identify the sharp-interface limit, that is the limit when letting the diffuse-interface width go to zero. Notably the upscaling and the sharp-interface limit commute. The numerical examples discussed in § 7 conclude the work.

2. The sharp-interface model

We start by presenting the sharp-interface model, which is then approximated by a phase-field model. For both the sharp-interface model and the phase-field model see Rohde & von Wolff (2021) for more details. We let $T > 0$ stand for the maximal time. For each $t \in [0, T]$, an N-dimensional domain Ω ($N = 2$ or 3) is partitioned into three disjoint subdomains, $\Omega_1(t)$, $\Omega_2(t)$ and $\Omega_3(t)$. These are occupied by the two fluid phases and by the solid phase, respectively. The interface between the domain Ω_i and Ω_j is denoted by Γ_{ij} ($i, j \in \{1, 2, 3\}$, $i \neq j$). Observe that these interfaces also depend on time.

https://doi.org/10.1017/jfm.2022.308 Published online by Cambridge University Press

With $t \in (0, T]$, in the fluid occupied subdomains $\Omega_i(t)$, $i \in \{1, 2\}$ the model is governed by the incompressible Navier–Stokes equations

$$\nabla \cdot \boldsymbol{v} = 0, \tag{2.1}$$

$$\partial_t(\rho_i \boldsymbol{v}) + \nabla \cdot (\rho_i \boldsymbol{v} \otimes \boldsymbol{v}) + \nabla p = \nabla \cdot (2\gamma_i \nabla^s \boldsymbol{v}), \tag{2.2}$$

where ρ_i, γ_i denote the mass density, respectively viscosity of the fluid phase i, all assumed constant here; $\boldsymbol{v}$ and p denote the fluid velocity and pressure in Ω_i, the index i being skipped. The symmetrized strain (Jacobian) is given by $\nabla^s \boldsymbol{v} = \frac{1}{2}(\nabla \boldsymbol{v} + (\nabla \boldsymbol{v})^t)$.

At the interface $\Gamma_{12}(t)$ (separating $\Omega_1(t)$ and $\Omega_2(t)$) we assume that the velocity $\boldsymbol{v}$ is continuous and that the jump in the normal stress is only in the normal direction, and proportional to the curvature of the interface

$$[\![\boldsymbol{v}]\!] = 0, \tag{2.3}$$

$$[\![(pI - 2\gamma \nabla^s \boldsymbol{v}) \cdot \boldsymbol{n}]\!] = \sigma_{12} \kappa \boldsymbol{n}, \tag{2.4}$$

$$v = \boldsymbol{v} \cdot \boldsymbol{n}. \tag{2.5}$$

Here, $[\![\cdot]\!]$ denotes the jump of a quantity over the interface, $\boldsymbol{n}$ the unit normal vector pointing outwards Ω_1, κ the curvature of the interface and σ_{12} the constant surface tension coefficient. Through the last condition, the normal velocity v of the interface and the normal velocity of the fluids are equal.

The subdomain $\Omega_3(t)$ is occupied by a mineral. We assume that the mineral phase is non-deforming and always connected to an outer boundary. Therefore, the mineral phase is stationary, and we do not need to solve for a velocity field $\boldsymbol{v}$ here. Note that this does not allow for small mineral grains that are transported by the fluid flow. The mineral phase is formed by the precipitation of two solute species present in fluid 1. The reverse process, in which the mineral can be dissolved and release solute in fluid 1 is also possible. In a simplified setting, assuming a constant electrical charge, it suffices to consider only one solute concentration in the model (see van Duijn & Knabner 1997), which is denoted by c. Here, we assume that solute is only present in fluid 1. Therefore, the solute transport is governed by the transport–diffusion equation in $\Omega_1(t)$

$$\partial_t c + \nabla \cdot (\boldsymbol{v} c) - D\Delta c = 0, \tag{2.6}$$

where D is the constant diffusion coefficient.

The interface $\Gamma_{13}(t)$ is evolving due to precipitation and dissolution. At Γ_{13} one has

$$v = -r(c) + \alpha \sigma_{13} \kappa, \tag{2.7}$$

$$D\nabla c \cdot \boldsymbol{n} = v(c^* - c). \tag{2.8}$$

The reaction rate $r(c)$ appearing in the former is generic and only depending on the solute concentration c. It accounts for dissolution and precipitation effects and is assumed increasing in c. In a more general situation we would expect the reaction rate to also depend on temperature. For the sake of simplicity we focus on the isothermal case here.

Remark 2.1. A simple reaction rate $r(c)$ can be constructed by assuming a constant dissolution rate k_1 and a quadratic mass action law, with rate k_2, for precipitation. With this the reaction rate is given by

$$r(c) = -k_1 + k_2 c^2. \tag{2.9}$$

https://doi.org/10.1017/jfm.2022.308 Published online by Cambridge University Press

The last term in (2.7), involving a constant parameter $\alpha \geq 0$ and the constant surface energy σ_{13}, allows for curvature effects in the evolution of Γ_{13}, e.g. an accelerated dissolution of solid tips peaking into the fluid phase. For $\alpha = 0$ no curvature effects enter the model.

Equation (2.8) is the Rankine–Hugoniot condition, ensuring the conservation of the solute species c. Here, c^* is the (constant) molar concentration of the solute species, now as part of the mineral phase Ω_3. We refer to van Noorden (2009*a*) for the mathematical modelling details. For a specific application, we refer to von Wolff *et al.* (2021), where calcite precipitation is studied. There, c denotes the molar concentration of inorganic carbon in the fluid, and c^* is the molar density of calcium carbonate.

Equations (2.7) and (2.8) only hold at $\Gamma_{13}(t)$ and not at outer boundaries of Ω. That is, we do not allow for precipitation and dissolution at the outer boundaries of Ω.

At the fluid–fluid interface $\Gamma_{12}(t)$, a similar Rankine–Hugoniot condition is imposed

$$\nabla c \cdot \boldsymbol{n} = 0. \tag{2.10}$$

As before, $\boldsymbol{n}$ is the unit normal vector pointing outwards Ω_1. This condition ensures conservation of the solute c, since the concentration c in fluid 2 is zero, and the normal velocity of the two fluids and of the interface are equal.

In contrast to Γ_{13}, no precipitation or dissolution are possible at the interface Γ_{23} between Ω_2 and Ω_3. This is because we assume that fluid 2 does not contain any solute species. Therefore, the interface does not evolve, and its normal velocity is $v = 0$.

At the interfaces between a fluid and the mineral we impose the no-penetration condition

$$\boldsymbol{v} \cdot \boldsymbol{n} = 0, \tag{2.11}$$

at Γ_{12} and Γ_{23}.

Remark 2.2. Equation (2.11) ensures conservation of mass, under the following assumptions. First, we assume that the concentration of ions in the first fluid is small, so the mass density ρ_1 of this fluid phase is constant. Moreover, we assume that ρ_1 also equals the mass density ρ_3 of the solid phase. In the more general case of $\rho_1 \neq \rho_3$, a volume change associated with the reaction may appear, and one obtains the more general interface condition

$$-\rho_1 \boldsymbol{v} \cdot \boldsymbol{n} = v[\![\rho]\!], \tag{2.12}$$

at Γ_{12} and Γ_{23}. We refer to van Noorden (2009*a*) for more details on this aspect. For the sake of simplicity and because we assume that the normal velocity v of the fluid–solid interfaces is small, we will present the simplified case of (2.11).

Finally, at the interfaces between a fluid and the mineral a Navier-slip condition (see Navier 1823) is assumed,

$$\boldsymbol{v} \cdot \tau = -2L_{slip}\tau(\nabla^s \boldsymbol{v})\boldsymbol{n}, \tag{2.13}$$

at Γ_{i3} ($i \in \{1, 2\}$). Here, $\tau \in \mathbb{R}^N$ is any tangent vector to Γ_{i3} (thus $\tau \perp \boldsymbol{n}$). The slip length $L_{slip} \geq 0$ is given by

$$L_{slip} = \gamma_1 \sqrt{\frac{2}{\rho_3 d_0 \gamma_3}}. \tag{2.14}$$

https://doi.org/10.1017/jfm.2022.308 Published online by Cambridge University Press

Here, ρ_3 is the density of the solid phase, and the constant d_0 will be determined by choices in the phase-field model. As explained in Rohde & von Wolff (2021), γ_3 is not the viscosity of the solid phase, but can be chosen instead to archive a given slip length L_{slip} in the relation (2.14). While the model allows for a positive slip length to account for additional properties of the fluid–solid interface, e.g. surface roughness, one can also choose γ_3 large enough to get $L_{slip} \approx 0$.

As a last step we consider points where the fluid–fluid interface Γ_{12} intersects the solid boundary $\Gamma_{13} \cup \Gamma_{23}$. At these contact points all bulk domains $\Omega_1, \Omega_2, \Omega_3$ meet. We assume that the set of contact points consist of distinct points when in two dimensions and of distinct lines in the three-dimensional case. We focus first on the two-dimensional case.

Given the constant surface energies $\sigma_{12}, \sigma_{13}, \sigma_{23} > 0$ we impose for the contact angle the condition

$$\frac{\sin(\beta_1)}{\sigma_{23}} = \frac{\sin(\beta_2)}{\sigma_{13}} = \frac{\sin(\beta_3)}{\sigma_{12}}, \tag{2.15}$$

with β_i being the contact angle of phase Ω_i at the contact point. Together with the condition $\beta_1 + \beta_2 + \beta_3 = 2\pi$ this uniquely determines the contact angles β_i. In the three-dimensional case, the same condition (2.15) is imposed on the plane perpendicular to the contact line.

3. The phase-field model

The sharp-interface model in § 2 involves free boundaries, which makes it difficult from both the analysis and numerical points of view. Relying on the idea to approximate the characteristic functions of each of the phases by smooth phase indicators (Caginalp & Fife 1988), phase-field models are convenient alternatives. For the specific problem considered here, a phase-field model called δ-$2f1s$-model was introduced in Rohde & von Wolff (2021); here, we present it briefly for completeness. We refer to Rohde & von Wolff (2021) for more details on the derivation and the properties of the model, including the derivation of the sharp-interface limit.

3.1. *Preliminaries*

The δ-$2f1s$-model introduces three phase-field variables ϕ_1, ϕ_2, ϕ_3 that represent the volume fraction of the two fluid phases and of the solid phase, respectively. Thus, ϕ_i approximates the indicator function of Ω_i appearing in the sharp-interface model in § 2. The phase-field variables $\boldsymbol{\Phi} = (\phi_1, \phi_2, \phi_3)^t$ are smooth and defined on the entire domain Ω. In the sharp-interface model, the transition from one phase to another is across an interface. In the phase-field model, this interface is replaced by a diffuse transition zone from one phase to another, where the gradients of the corresponding phase-field variables are high. A ternary Cahn–Hilliard equation governs the evolution of $\boldsymbol{\Phi}$, and is coupled with a Navier–Stokes equation for fluid flow, and a reaction–transport–diffusion equation for dissolved ion concentration c.

The δ-$2f1s$-model additionally introduces a small regularization parameter $\delta > 0$. Since no maximum principle holds for the Cahn–Hilliard equation, δ is used to ensure the

https://doi.org/10.1017/jfm.2022.308 Published online by Cambridge University Press

positivity of the volume fractions. Also, the double-well potential

$$W_{dw}(\phi) = 450\phi^4(1-\phi)^4 + \delta\ell\left(\frac{\phi}{\delta}\right) + \delta\ell\left(\frac{1-\phi}{\delta}\right),$$
$$\text{with } \ell(x) = \begin{cases} \dfrac{x^2}{1+x} & x \in (-1, 0), \\ 0 & x \geq 0, \end{cases} \tag{3.1}$$

is employed. Observe that W_{dw} has two minima at 0 and 1, and becomes unbounded at $-\delta$ and $1+\delta$. With this, we define the triple-well potential

$$W(\boldsymbol{\Phi}) := W_0(P\boldsymbol{\Phi}), \quad \text{where } W_0(\boldsymbol{\Phi}) = \sum_{i=1}^{3} \Sigma_i W_{dw}(\phi_i). \tag{3.2}$$

Here, $\Sigma_i > 0$ are surface energy coefficients, and P is the projection of $\mathbb{R}^3$ onto the plane $\sum_i \phi_i = 1$, given by

$$P\boldsymbol{\Phi} = \boldsymbol{\Phi} + \Sigma_T(1-\phi_1-\phi_2-\phi_3)\begin{pmatrix} \Sigma_1^{-1} \\ \Sigma_2^{-1} \\ \Sigma_3^{-1} \end{pmatrix}, \quad \frac{1}{\Sigma_T} = \frac{1}{\Sigma_1} + \frac{1}{\Sigma_2} + \frac{1}{\Sigma_3}. \tag{3.3a,b}$$

As shown in Rohde & von Wolff (2021), this construction ensures that the volume fractions sum to one, i.e. $\sum_{i=1}^{3} \phi_i = 1$, provided the initial data have this property. Furthermore, Rohde & von Wolff (2021) uses an energy argument and the unboundedness of the potential to show that $-\delta < \phi_i < 1+\delta$ $(i = 1, 2, 3)$.

Next, we define the total fluid volume fraction $\tilde{\phi}_f$ and ion-dissolving fluid fraction ϕ_c as

$$\tilde{\phi}_f := \phi_1 + \phi_2 + 2\delta\phi_3, \tag{3.4}$$
$$\phi_c := \phi_1, \tag{3.5}$$
$$\tilde{\phi}_c := \phi_1 + \delta. \tag{3.6}$$

Here, the tilde denotes a modification using the small parameter δ, to ensure that the respective variables are positive. Using the (constant) fluid densities ρ_i and viscosities γ_i the total fluid density ρ_f and viscosity $\tilde{\gamma}$ become

$$\rho_f(\boldsymbol{\Phi}) := \rho_1\phi_1 + \rho_2\phi_2, \tag{3.7}$$
$$\tilde{\rho}_f(\boldsymbol{\Phi}) := \rho_1\phi_1 + \rho_2\phi_2 + (\rho_1+\rho_2)\delta, \tag{3.8}$$
$$\tilde{\gamma}(\boldsymbol{\Phi}) := (\phi_1\gamma_1^{-1} + \phi_2\gamma_2^{-1} + \phi_3\gamma_3^{-1} + (\gamma_1^{-1} + \gamma_2^{-1} + \gamma_3^{-1})\delta)^{-1}. \tag{3.9}$$

3.2. *The δ-2f1s-model*

We now present the δ-2f1s-model. All equations are defined in $(0, T] \times \Omega$. The flow is governed by the Navier–Stokes equations and involves the fluid fraction $\tilde{\phi}_f$,

$$\nabla \cdot (\tilde{\phi}_f \boldsymbol{v}) = 0, \tag{3.10}$$
$$\partial_t(\tilde{\rho}_f \boldsymbol{v}) + \nabla \cdot ((\rho_f \boldsymbol{v} + \rho_1 \boldsymbol{J}_1 + \rho_2 \boldsymbol{J}_2) \otimes \boldsymbol{v}) = -\tilde{\phi}_f \nabla p + \nabla \cdot (2\tilde{\gamma}(\boldsymbol{\Phi})\nabla^s \boldsymbol{v}) - \rho_3 d(\tilde{\phi}_f)\boldsymbol{v} + \tilde{\boldsymbol{S}} + \frac{1}{2}\rho_1 \boldsymbol{v} R. \tag{3.11}$$

https://doi.org/10.1017/jfm.2022.308 Published online by Cambridge University Press

This is coupled with the transport–diffusion–reaction equation for the ion concentration

$$\partial_t(\tilde{\phi}_c c) + \nabla \cdot ((\phi_c \boldsymbol{v} + \boldsymbol{J}_1)c) = D\nabla \cdot (\tilde{\phi}_c \nabla c) + c^* R. \tag{3.12}$$

The phase-field variables ϕ_1, ϕ_2, ϕ_3 satisfy the Cahn–Hilliard equations

$$\partial_t \phi_1 + \nabla \cdot (\phi_1 \boldsymbol{v} + \boldsymbol{J}_1) = R, \tag{3.13}$$

$$\partial_t \phi_2 + \nabla \cdot (\phi_2 \boldsymbol{v} + \boldsymbol{J}_2) = 0, \tag{3.14}$$

$$\partial_t \phi_3 + \nabla \cdot (2\delta\phi_3 \boldsymbol{v} + \boldsymbol{J}_3) = -R, \tag{3.15}$$

$$\boldsymbol{J}_i = -\frac{\varepsilon M}{\Sigma_i} \nabla \mu_i, \quad i \in \{1, 2, 3\}, \tag{3.16}$$

$$\mu_i = \frac{\partial_{\phi_i} W(\boldsymbol{\Phi})}{\varepsilon} - \varepsilon \Sigma_i \Delta \phi_i, \quad i \in \{1, 2, 3\}. \tag{3.17}$$

Compared with the common Navier–Stokes equations, some modifications appear in (3.11). The fluid density $\tilde{\rho}_f(\boldsymbol{\Phi})$ introduces a strong coupling between the Navier–Stokes equations and the Cahn–Hilliard equations. All terms except the advection term use the modified quantities $\tilde{\phi}_f$, $\tilde{\rho}_f$ and $\tilde{\gamma}$. Additional flux terms $\rho_i \boldsymbol{J}_i \otimes \boldsymbol{v}$ are introduced to account for momentum fluxes due to the Cahn–Hilliard evolution. Secondly, the dissipative term $-\rho_3 d(\tilde{\phi}_f)\boldsymbol{v}$ is added. Here, d is a decreasing function such that $d(0) = d_0 > 0$ and $d(1) = 0$, for example $d(\tilde{\phi}_f) = d_0(1 - \tilde{\phi}_f)^2$. The term $d(\tilde{\phi}_f)$ is therefore active in the solid phase and guarantees that $\boldsymbol{v}$ remains small there. It also influences the slip length L_{slip}. Lastly, the surface tension term $\tilde{\boldsymbol{S}}$ is given by

$$\tilde{\boldsymbol{S}} = -\mu_2 \tilde{\phi}_f \nabla \left(\frac{\phi_1}{\tilde{\phi}_f} \right) - \mu_1 \tilde{\phi}_f \nabla \left(\frac{\phi_2}{\tilde{\phi}_f} \right) - 2\delta\phi_3 \nabla(\mu_3 - \mu_1 - \mu_2). \tag{3.18}$$

The reaction term R modelling precipitation and dissolution of ions is given by

$$R = -q(\boldsymbol{\Phi})(r(c) + \tilde{\alpha}\mu_1 - \tilde{\alpha}\mu_3). \tag{3.19}$$

Here, $r(c)$ is the increasing reaction rate used in the sharp-interface description (2.7). Additionally, the precipitation process can depend on curvature effects through surface effects that are similar to surface diffusion, and are encountered if $\alpha > 0$. Again, the tilde denotes a modification of α, that is $\tilde{\alpha} = \alpha + \delta$. Finally, to concentrate the reaction inside the diffuse interface region between fluid phase 1 and the solid phase, which is equivalent to the assumption made in the sharp-interface model, the non-dimensional term $q(\boldsymbol{\Phi}) = 30\phi_1^2\phi_3^2$ is used. Observe that q dominates wherever neither ϕ_1 nor ϕ_2 are close to 0, which is precisely the envisaged location for the fluid 1–mineral interface.

4. Non-dimensionalization

We proceed by bringing the δ-2f1s-model (3.10)–(3.17) to a non-dimensional form, and derived an upscaled counterpart of it by employing asymptotic expansion and averaging techniques. We consider a simplified geometric setting. We start by introducing a thin strip having length L and width $\ell \ll L$, as shown in figure 1.

With a chosen domain width $\ell_\Omega > \ell$, the domain $\Omega = [0, L] \times [-\ell_\Omega/2, \ell_\Omega/2]$ includes the thin strip mentioned above, which is identified as $[0, L] \times [-\ell/2, \ell/2]$. The region outside the strip is occupied by the mineral, so $\boldsymbol{\Phi} \approx (0, 0, 1)^t$ there. The diffuse

https://doi.org/10.1017/jfm.2022.308 Published online by Cambridge University Press

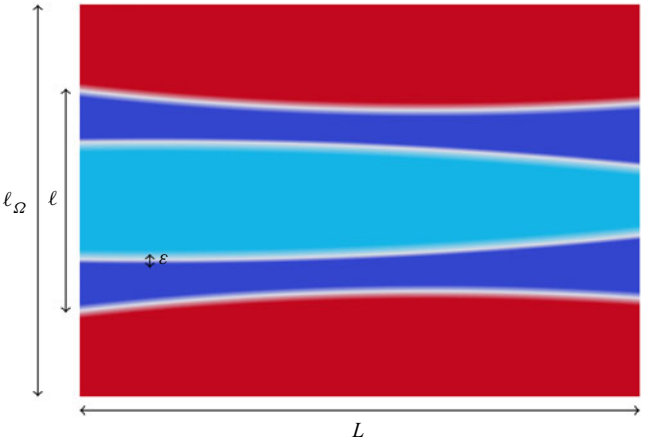

Figure 1. Setting of the thin strip: the strip with length L and width ℓ consists of solid walls (red, $\boldsymbol{\Phi} \approx (0, 0, 1)^t$) and fluid phases (light blue, dark blue). The diffuse-interface width ε is smaller than ℓ.

interfaces are located in regions of width ε. We assume here that the diffuse-interface regions remain clearly separated inside the thin strip, hence $\varepsilon \ll \ell$.

Three length scales can be identified, $L \gg \ell \gg \varepsilon$. These are related through the aspect ratio $\beta = \ell/L$ and the Cahn number $Cn = \varepsilon/L$, both assumed small. Observe that, in fact, $Cn \ll \beta \ll 1$.

The reference quantities used in the non-dimensionalization procedure are listed in table 1. Non-dimensional values are then identified by a hat. Note that we relate only few reference values directly to each other. In particular, we do relate reference values when we want to emphasize an explicit dependence on y_{ref}, as seen for p_{ref}, d_{ref} and μ_{ref}. The choices are motivated as follows. To obtain an upscaled macroscopic velocity of order $v_{ref} = x_{ref}/t_{ref}$, the pressure drop in the thin strip has to scale with $1/(y_{ref})^2$. Also, the slip length L_{slip} is supposed to be of order ℓ and not L, which is achieved by a momentum dissipation scaling $1/(y_{ref})^2$.

We rewrite the Cahn number introduced above in terms of reference quantities, and define other dimensionless numbers that are used below to relate the reference quantities: the Reynolds number, Capillary number, Damköhler number and Péclet numbers of the Cahn–Hilliard (CH) evolution and ion concentration

$$\left.\begin{aligned} Re = \frac{\rho_{ref} v_{ref} x_{ref}}{\gamma_{ref}}, \quad Ca = \frac{\gamma_{ref} v_{ref}}{\Sigma_{ref}}, \quad Cn = \frac{\varepsilon_{ref}}{x_{ref}}, \\ Da = \frac{r_{ref} x_{ref}}{v_{ref}}, \quad Pe_{CH} = \frac{v_{ref} x_{ref}}{M_{ref}}, \quad Pe_c = \frac{v_{ref} x_{ref}}{D_{ref}}. \end{aligned}\right\} \tag{4.1}$$

Clearly, the non-dimensionalization also affects the spatial and temporal derivatives, namely

$$\hat{\nabla} = x_{ref} \nabla \quad \text{and} \quad \partial_{\hat{t}} = t_{ref} \partial_t. \tag{4.2a,b}$$

We now can insert the non-dimensional variables of table 1, the non-dimensional numbers (4.1) and the non-dimensional operators in (4.2a,b) into the δ-2f1s-model

https://doi.org/10.1017/jfm.2022.308 Published online by Cambridge University Press

Variable	Reference value	Non-dimensional variable
time	$t_{ref} = T$	$\hat{t} = t/t_{ref}$
space	$x_{ref} = L$,	$\hat{x} = x/x_{ref}$
	$y_{ref} = \ell$,	$\hat{y} = y/y_{ref}$
	$\varepsilon_{ref} = \varepsilon$	$\hat{\varepsilon} = 1$
velocity	$v_{ref} = x_{ref}/t_{ref}$	$\hat{\boldsymbol{v}} = \boldsymbol{v}/v_{ref}$
density	$\rho_{ref} = \rho_1$	$\hat{\rho}_i = \rho_i/\rho_{ref}, i \in \{1, 2, 3\}$
		$\hat{\rho}_f = \rho_f/\rho_{ref}$
		$\hat{\tilde{\rho}}_f = \tilde{\rho}_f/\rho_{ref}$
viscosity	$\gamma_{ref} = \gamma_1$	$\hat{\gamma}_i = \gamma_i/\gamma_{ref}, i \in \{1, 2, 3\}$
		$\hat{\tilde{\gamma}} = \tilde{\gamma}/\gamma_{ref}$
pressure	$p_{ref} = \gamma_{ref} v_{ref} x_{ref}/(y_{ref})^2$	$\hat{p} = p/p_{ref}$
momentum dissipation rate	$d_{ref} = \gamma_{ref}/(\rho_{ref} y_{ref}^2)$	$\hat{d} = d/d_{ref}$
surface energy	$\Sigma_{ref} = \Sigma_1$	$\hat{\Sigma}_i = \Sigma_i/\Sigma_{ref}, i \in \{1, 2, 3\}$
CH mobility	$M_{ref} = M$	$\hat{M} = 1$
CH chemical potential	$\mu_{ref} = \Sigma_{ref}/y_{ref}$	$\hat{\mu} = \mu/\mu_{ref}$
CH triple-well potential	$W_{ref} = \Sigma_{ref}$	$\hat{W} = W/\Sigma_{ref}$
molar concentration	$c_{ref} = c^*$	$\hat{c} = c/c_{ref}$
diffusion coefficient	$D_{ref} = D$	$\hat{D} = 1$
reaction rate	r_{ref}	$\hat{r}(\hat{c}) = r(c)/r_{ref}$
interface-reaction diffusivity	$\alpha_{ref} = r_{ref}/\mu_{ref}$	$\hat{\alpha} = \alpha/\alpha_{ref}$

Table 1. Variables, reference values and non-dimensional quantities for the non-dimensionalization.

(3.10)–(3.17). The non-dimensional equations become

$$\hat{\boldsymbol{\nabla}} \cdot (\tilde{\phi}_f \hat{\boldsymbol{v}}) = 0, \tag{4.3}$$

$$\begin{aligned} &\partial_{\hat{t}}(\hat{\tilde{\rho}}_f \hat{\boldsymbol{v}}) + \hat{\boldsymbol{\nabla}} \cdot (\hat{\rho}_f \hat{\boldsymbol{v}} \otimes \hat{\boldsymbol{v}}) + \frac{Cn}{\beta Pe_{CH}} \hat{\boldsymbol{\nabla}} \cdot ((\hat{\rho}_1 \hat{\boldsymbol{J}}_1 + \hat{\rho}_2 \hat{\boldsymbol{J}}_2) \otimes \hat{\boldsymbol{v}}) \\ &\quad = -\frac{1}{\beta^2 Re} \tilde{\phi}_f \hat{\boldsymbol{\nabla}} \hat{p} + \frac{1}{Re} \hat{\boldsymbol{\nabla}} \cdot (2\hat{\tilde{\gamma}}(\boldsymbol{\Phi}) \hat{\nabla}^s \hat{\boldsymbol{v}}) \\ &\qquad - \frac{1}{\beta^2 Re} \hat{\rho}_3 \hat{d}(\tilde{\phi}_f) \hat{\boldsymbol{v}} + \frac{1}{\beta Re} \frac{1}{Ca} \hat{\tilde{\boldsymbol{S}}} + Da \frac{1}{2} \hat{\rho}_1 \hat{\boldsymbol{v}} \hat{R}, \end{aligned} \tag{4.4}$$

for the flow,

$$\partial_{\hat{t}}(\tilde{\phi}_c \hat{c}) + \hat{\boldsymbol{\nabla}} \cdot (\phi_c \hat{\boldsymbol{v}} \hat{c}) + \frac{Cn}{\beta Pe_{CH}} \hat{\boldsymbol{\nabla}} \cdot (\hat{\boldsymbol{J}}_1 \hat{c}) = \frac{1}{Pe_c} \hat{\boldsymbol{\nabla}} \cdot (\tilde{\phi}_c \hat{\boldsymbol{\nabla}} \hat{c}) + Da \hat{R}, \tag{4.5}$$

for the ion transport–diffusion–reaction, while for the Cahn–Hilliard evolution one gets

$$\partial_{\hat{t}} \phi_1 + \hat{\boldsymbol{\nabla}} \cdot (\phi_1 \hat{\boldsymbol{v}}) + \frac{Cn}{\beta Pe_{CH}} \hat{\boldsymbol{\nabla}} \cdot \hat{\boldsymbol{J}}_1 = Da \hat{R}, \tag{4.6}$$

$$\partial_{\hat{t}} \phi_2 + \hat{\boldsymbol{\nabla}} \cdot (\phi_2 \hat{\boldsymbol{v}}) + \frac{Cn}{\beta Pe_{CH}} \hat{\boldsymbol{\nabla}} \cdot \hat{\boldsymbol{J}}_2 = 0, \tag{4.7}$$

$$\partial_{\hat{t}} \phi_3 + \hat{\boldsymbol{\nabla}} \cdot (2\delta \phi_3 \hat{\boldsymbol{v}}) + \frac{Cn}{\beta Pe_{CH}} \hat{\boldsymbol{\nabla}} \cdot \hat{\boldsymbol{J}}_3 = -Da \hat{R}, \tag{4.8}$$

https://doi.org/10.1017/jfm.2022.308 Published online by Cambridge University Press

$$\hat{\boldsymbol{J}}_i = -\frac{1}{\hat{\Sigma}_i}\hat{\nabla}\hat{\mu}_i, \quad i \in \{1, 2, 3\}, \tag{4.9}$$

$$\frac{\hat{\mu}_i}{\beta} = \frac{\partial_{\phi_i}\hat{W}(\boldsymbol{\Phi})}{Cn} - Cn\hat{\Sigma}_i\hat{\nabla}^2\phi_i, \quad i \in \{1, 2, 3\}. \tag{4.10}$$

All equations are defined in the dimensionless time–space domain $(0, 1] \times \hat{\Omega}$, where $\hat{\Omega} = [0, 1] \times [-\hat{\ell}_\Omega/2, \hat{\ell}_\Omega/2]$. The surface tension and reaction are given as

$$\hat{\tilde{\boldsymbol{S}}} = -\hat{\mu}_2\tilde{\phi}_f\hat{\nabla}\left(\frac{\phi_1}{\tilde{\phi}_f}\right) - \hat{\mu}_1\tilde{\phi}_f\hat{\nabla}\left(\frac{\phi_2}{\tilde{\phi}_f}\right) - 2\delta\phi_3\hat{\nabla}(\hat{\mu}_3 - \hat{\mu}_1 - \hat{\mu}_2), \tag{4.11}$$

$$\hat{R} = -q(\boldsymbol{\Phi})(\hat{r}(\hat{c}) + \hat{\tilde{\alpha}}\hat{\mu}_1 - \hat{\tilde{\alpha}}\hat{\mu}_3). \tag{4.12}$$

From here on, we will only work with the non-dimensional model and therefore the hats are left out in the notation.

5. Upscaling in a thin strip

We now proceed by deriving the upscaled model, obtained when passing to the limit $\beta \to 0$. This means that the thin strip reduces to a one-dimensional object, as its width is vanishing compared with its length.

We introduce new coordinates (x, y) such that $\boldsymbol{x} = (x, \beta y)$. In the thin strip we expect all variables to vary in the longitudinal direction $\boldsymbol{e}_x$ on the length scale $L = x_{ref}$ and in the transverse direction $\boldsymbol{e}_y$ on the length scale $\ell = y_{ref} = \beta x_{ref}$. In particular, this will result in $\nabla = \boldsymbol{e}_x\partial_x + \beta^{-1}\boldsymbol{e}_y\partial_y$.

The non-dimensional domain is given by $\Omega = [0, 1] \times [-\ell_\Omega/2, \ell_\Omega/2]$ (recall that we dropped the hats in the notation) and we choose for the upscaling the boundary conditions at $y = \pm\ell_\Omega/2$ as

$$\partial_y\boldsymbol{\Phi}(t, x, \pm\ell_\Omega/2) = 0, \tag{5.1}$$

$$\partial_y\mu(t, x, \pm\ell_\Omega/2) = 0, \tag{5.2}$$

$$\partial_y c(t, x, \pm\ell_\Omega/2) = 0, \tag{5.3}$$

$$\boldsymbol{v}(t, x, \pm\ell_\Omega/2) = 0. \tag{5.4}$$

5.1. *Scaling of non-dimensional numbers*

The upscaled model will also depend on the scaling of the dimensionless numbers (4.1) with respect to β. We consider the following behaviour of these numbers with respect to β

$$Re = \overline{Re}, \tag{5.5}$$

$$Ca = \overline{Ca}, \tag{5.6}$$

$$Cn = \beta\bar{\varepsilon}, \tag{5.7}$$

$$Da = \overline{Da}/\bar{\varepsilon}, \tag{5.8}$$

$$Pe_{CH} = 1/(\beta^2\bar{M}), \tag{5.9}$$

$$Pe_c = \overline{Pe_c}, \tag{5.10}$$

where $\overline{Re}, \overline{Ca}, \bar{\varepsilon}, \overline{Da}, \bar{M}, \overline{Pe_c}$ are constants independent of β. In detail, these choices are motivated as follows.

https://doi.org/10.1017/jfm.2022.308 Published online by Cambridge University Press

- The moderate Reynolds number (5.5) leads to a parabolic flow profile in the thin strip, we expect laminar flow.
- As the curvature of the fluid–fluid interface is of order $O(\beta)$, choosing a moderate capillary number Ca in (5.6) leads to the same pressure in both fluids, thus the capillary pressure becomes 0 (for sharp-interface models see also Sharmin *et al.* 2020; Lunowa *et al.* 2021). Note that this is a major difference to the three-dimensional case (see e.g. Mikelić 2009) where we expect a curvature of $O(\beta^{-1})$ leading to a non-zero capillary pressure.
- The scaling of the Cahn number Cn in (5.7) can be reformulated to $\bar{\varepsilon} = \varepsilon/\ell$. Therefore, the interface width ε scales with the width of the thin strip, ℓ. At the same time, the diffuse-interface regions are assumed to be localized inside the thin strip, therefore we require $\varepsilon \ll \ell$. This translates into a fixed, small $\bar{\varepsilon}$, i.e. $\bar{\varepsilon} \ll 1$. In the numerical experiments presented in § 7 we choose $\bar{\varepsilon} = 0.03$.
- We consider a moderate Damköhler number (5.8). In the sharp-interface model, this would ensure that the interfaces move with moderate velocity inside the thin strip, proportional to ℓ/T. In the diffuse-interface model, the reaction is only active in the diffuse-interface region, which has an area scaling with ε. Therefore, Da is divided by $\bar{\varepsilon}$, and expect to have fluid–solid or fluid–fluid interfaces evolving over the length scale ℓ. A dominating Damk' ohler regime like $Da = O(\beta^{-1})$ would instead lead to equilibrium-type reactions in the upscaled model, but the evolution of the interfaces should remain moderate. This can be achieved by assuming that the molar density of the species in the precipitate is sufficiently high to compensate the fast reaction kinetics.
- The high Péclet number (5.9) for the phase field assures that the evolution of the phase field remains within the transverse length scale ℓ in an $O(1)$ time scale.
- The moderate Péclet number of the ion diffusion (5.10) will result in a macroscopic diffusion of ions, while the ion distribution in the transverse direction equilibrates faster than the $O(1)$ time scale.

Lastly, the small, non-dimensional number $\delta > 0$ appears in the δ-2f1s-model. It is used as a regularization parameter, to ensure the positivity of volume fractions, density and viscosity. Here, we assume that δ is constant and independent of β.

5.2. *Asymptotic expansions*

We assume that we can write solutions to the non-dimensional δ-2f1s-model (4.3)–(4.10) in terms of an asymptotic expansion in β of $\boldsymbol{\Phi}, \boldsymbol{v}, p, c, \mu_1, \mu_2, \mu_3$. To be precise, we assume expansions of the form

$$\boldsymbol{\Phi}(t, \boldsymbol{x}) = \boldsymbol{\Phi}_0(t, x, y) + \beta \boldsymbol{\Phi}_1(t, x, y) + \beta^2 \boldsymbol{\Phi}_2(t, x, y) + \cdots, \tag{5.11}$$

where $\boldsymbol{\Phi}_k, k \in \mathbb{N}_0$ does not depend on β.

Inserting these asymptotic expansions into the non-dimensional δ-2f1s-model we group by powers of β. As the calculations are lengthy, we show them in Appendix A.

Remark 5.1. Note that the asymptotic expansions are written depending on the new coordinates x and y. This means that in the $\boldsymbol{e}_x$ direction variables cannot vary on the (non-dimensional) length scale β, because a non-trivial function $f(x/\beta)$ cannot be expanded in the form $f(x/\beta) = f_0(x) + \beta f_1(x) + \cdots$. In particular, this implies that there are no phase-field interfaces possible perpendicular to the thin strip, as they would change

https://doi.org/10.1017/jfm.2022.308 Published online by Cambridge University Press

the value of $\boldsymbol{\Phi}$ over the length $Cn = \beta\bar{\varepsilon}$. We will discuss in § 7.2 a numerical example that violates this assumption.

The assumption is also violated for triple points, where all three phases meet, and for points where interfaces meet the boundary of Ω at $y = \pm\ell_\Omega/2$. Therefore, ℓ_Ω has to be chosen big enough, such that the width of the thin strip does not reach ℓ_Ω.

We will present in § 8 some ideas to handle cases where the assumption of slow variation in the $\boldsymbol{e}_x$ direction is violated.

5.3. *The upscaled δ-2f1s-model*

Let us summarize the results of the upscaling done in detail in Appendix A. Except for $\boldsymbol{v}$ we will only need the leading-order term of each unknown, and will therefore drop the subscript 0. We will call the model (5.12)–(5.27) the upscaled δ-2f1s-model.

From (A6) and (A21) we have the macroscopic continuity equation for the total flux Q_f and the Darcy equation for the pressure p, and the macroscopic transport–diffusion–reaction equation for the ion concentration c (A18)

$$\partial_x Q_f = 0, \tag{5.12}$$

$$Q_f = -K_f \partial_x p, \tag{5.13}$$

$$\frac{\mathrm{d}}{\mathrm{d}t}(\tilde{\phi}_{c,total} c) + \partial_x((-K_c \partial_x p)c) = \frac{1}{\overline{Pe_c}} \partial_x(\tilde{\phi}_{c,total} \partial_x c) + \frac{\overline{Da}}{\bar{\varepsilon}} R_{total}. \tag{5.14}$$

These equations are macroscopic in the sense that the unknowns Q_f, p and c depend only on x and t, but not on y. The parameters in these equations are upscaled quantities, depending on the exact distribution of the phases in the y direction

$$\tilde{\phi}_{c,total} = \int_{-\ell_\Omega/2}^{\ell_\Omega/2} \tilde{\phi}_c \,\mathrm{d}y, \tag{5.15}$$

$$K_f(t,x) = \int_{-\ell_\Omega/2}^{\ell_\Omega/2} \tilde{\phi}_f w \,\mathrm{d}y, \tag{5.16}$$

$$K_c(t,x) = \int_{-\ell_\Omega/2}^{\ell_\Omega/2} \tilde{\phi}_c w \,\mathrm{d}y, \tag{5.17}$$

$$R_{total} = \int_{-\ell_\Omega/2}^{\ell_\Omega/2} R \,\mathrm{d}y. \tag{5.18}$$

For the phase-field parameters we still have to solve the fully coupled two-dimensional problem (A7), (A9), (A10), (A11), that is

$$\partial_t \phi_1 + \partial_x(\phi_1 \boldsymbol{v}_0^{(1)}) + \partial_y(\phi_1 \boldsymbol{v}_1^{(2)}) - \frac{\bar{\varepsilon}\bar{M}}{\Sigma_1} \partial_y^2 \mu_1 = \frac{\overline{Da}}{\bar{\varepsilon}} R, \tag{5.19}$$

$$\partial_t \phi_2 + \partial_x(\phi_2 \boldsymbol{v}_0^{(1)}) + \partial_y(\phi_2 \boldsymbol{v}_1^{(2)}) - \frac{\bar{\varepsilon}\bar{M}}{\Sigma_2} \partial_y^2 \mu_2 = 0, \tag{5.20}$$

$$\partial_t \phi_3 + \partial_x(2\delta\phi_3 \boldsymbol{v}_0^{(1)}) + \partial_y(2\delta\phi_3 \boldsymbol{v}_1^{(2)}) - \frac{\bar{\varepsilon}\bar{M}}{\Sigma_3} \partial_y^2 \mu_3 = -\frac{\overline{Da}}{\bar{\varepsilon}} R, \tag{5.21}$$

$$\mu_i = \frac{\partial_{\phi_i} W(\boldsymbol{\Phi})}{\bar{\varepsilon}} - \bar{\varepsilon}\Sigma_i \partial_y^2 \phi_i, \quad i \in \{1,2,3\}, \tag{5.22}$$

https://doi.org/10.1017/jfm.2022.308 Published online by Cambridge University Press

with the reaction term

$$R = -q(\boldsymbol{\Phi})(r(c) + \tilde{\alpha}\mu_1 - \tilde{\alpha}\mu_3). \tag{5.23}$$

Note that, in contrast to the non-dimensional model (4.3)–(4.10), the Cahn–Hilliard evolution acts only in the $\boldsymbol{e}_y$ direction. The only term acting in the $\boldsymbol{e}_x$ direction is the transport of the fluid phases. This will enable us in § 7.1 to develop a numerical model that uses explicit upwinding for the fluid transport and can therefore decouple cell problems for different values of x.

For the flow it suffices to solve the cell problem (A22), (A23)

$$\rho_3 d(\tilde{\phi}_f)w - \partial_y(\tilde{\gamma}(\boldsymbol{\Phi})\partial_y w) = \tilde{\phi}_f, \tag{5.24}$$

$$\lim_{y \to \pm \ell_\Omega/2} w = 0, \tag{5.25}$$

and recover the flow $\boldsymbol{v}_0^{(1)}$, $\boldsymbol{v}_1^{(2)}$ by (A21) and (A5)

$$\boldsymbol{v}_0^{(1)} = -w\partial_x p, \tag{5.26}$$

$$\partial_x(\tilde{\phi}_f \boldsymbol{v}_0^{(1)}) + \partial_y(\tilde{\phi}_f \boldsymbol{v}_1^{(2)}) = 0. \tag{5.27}$$

Note that, while the equations for the flow (5.24)–(5.27) do not explicitly depend on time, they depend on the phase-field parameters $\boldsymbol{\Phi}$, which can change in time.

6. Sharp-interface limit of the upscaled δ-2f1s-model

In the previous section we have investigated the scale separation $\beta = \ell/L \to 0$. A different limit process that is commonly investigated for phase-field models is the sharp-interface limit $\varepsilon \to 0$. In Rohde & von Wolff (2021) this limit is analysed for the δ-2f1s-model (3.10)–(3.17), resulting in the sharp-interface evolution described in § 2.

Because the upscaled δ-2f1s-model (5.12)–(5.27) still contains a Cahn–Hilliard evolution, depending on the small number $\bar{\varepsilon} = \varepsilon/\ell$, we can investigate the sharp-interface limit $\bar{\varepsilon} \to 0$ of the upscaled δ-2f1s-model. This means that we are interested in the limit process of vanishing diffuse-interface width ε compared with the width ℓ of the thin strip. In the following, we will use matched asymptotic expansions to analyse this limit, the argumentation is mostly analogous to Rohde & von Wolff (2021).

6.1. *Assumptions and scaling of non-dimensional numbers*

To derive the sharp-interface limit $\bar{\varepsilon} \to 0$, we assume that $\overline{Pe_c}$, $\overline{Da}$, $\bar{M}$ are constant and independent of $\bar{\varepsilon}$. This choice of scaling allows for a reasonable limit process, with physical properties independent of the diffuse interface width.

The scaling $\delta = \bar{\varepsilon}$ is important. The regularization parameter δ is introduced in the δ-2f1s-model to ensure the positivity of e.g. the density $\tilde{\rho}_f(\boldsymbol{\Phi})$ in (3.8). This δ-regularization is not necessary for the sharp-interface formulation, and the choice $\delta = \bar{\varepsilon}$ leads to δ vanishing in the sharp-interface limit.

As a basic assumption we expect to have solutions that form bulk phases, characterized by nearly constant $\boldsymbol{\Phi}$, and interfaces, characterized by a large gradient of $\boldsymbol{\Phi}$. We also assume that $\mu_i, i \in \{1, 2, 3\}$ is of $O(1)$, not of $O(\bar{\varepsilon}^{-1})$, as (5.22) would suggest. For a discussion of why this assumption is reasonable on a $O(1)$ time scale, see Pego & Penrose (1989).

We also assume that in an interface between phase $\boldsymbol{\Phi} = \boldsymbol{e}_i$ and $\boldsymbol{\Phi} = \boldsymbol{e}_j$ the third phase is not present. This assumption is reasonable because with our constructions of W (3.2)

https://doi.org/10.1017/jfm.2022.308 Published online by Cambridge University Press

minimizers of the Ginzburg–Landau energy $W(\boldsymbol{\Phi}) + \sum_i \Sigma_i \Delta\phi_i$ that connect $\boldsymbol{\Phi} = \boldsymbol{e}_i$ and $\boldsymbol{\Phi} = \boldsymbol{e}_j$ satisfy $\phi_k = 0$, $k \in \{1, 2, 3\} \setminus \{i, j\}$.

As the calculations for the sharp-interface limit are lengthy, we present them in Appendix B. The sharp-interface limit consists of asymptotic expansions in the bulk phases (in the variables x and y), asymptotic expansions in the interface regions (in the variable x and a new variable z with characteristic length scale ε), and the matching of these asymptotic expansions.

6.2. *The upscaled sharp-interface model*

We will summarize the results of the matched asymptotic expansions presented in Appendix A. For this, we drop the subscript 0 and the superscript *out* for ease of notation. We call (6.1)–(6.19) the upscaled sharp-interface model.

The macroscopic equations for the unknowns Q_f, p and c are given by (B5), (B6) and (B9), that is

$$\partial_x Q_f = 0, \tag{6.1}$$

$$Q_f = -K_f \partial_x p, \tag{6.2}$$

$$\frac{\mathrm{d}}{\mathrm{d}t}(\phi_{c,total} c) + \partial_x((-K_c \partial_x p)c) = \frac{1}{\overline{Pe_c}} \partial_x(\phi_{c,total} \partial_x c) + \overline{Da} R_{interface}. \tag{6.3}$$

The coefficients of the upscaled equations depend on the distribution of the phases in the thin strip. In contrast to the upscaled phase-field model (5.12)–(5.27) the sharp-interface limit does not depend on the phase-field variables $\boldsymbol{\Phi}$. Instead, the three disjoint domains $\Omega_1(t)$, $\Omega_2(t)$ and $\Omega_3(t)$ are used to locate the phases. The interface between Ω_i and Ω_j is denoted by Γ_{ij}. We introduce the notation $\Omega_i|_x = \{y \in [-\ell_\Omega/2, \ell_\Omega/2] : (x, y) \in \Omega_i(t)\}$, and write $N(\Gamma_{13})$ for the number of Γ_{13} interfaces at a given x. With (B10), (B7), (B11) and (B53) we can calculate the coefficients of (6.1)–(6.3) as

$$\phi_{c,total}(x) = \mathrm{vol}(\Omega_1|_x), \tag{6.4}$$

$$K_f(t, x) = \int_{\Omega_1|_x \cup \Omega_2|_x} w \, \mathrm{d}y, \tag{6.5}$$

$$K_c(t, x) = \int_{\Omega_1|_x} w \, \mathrm{d}y, \tag{6.6}$$

$$R_{interface} = -N(\Gamma_{13}) r(c). \tag{6.7}$$

We describe the evolution of the phases with the interface velocity v. This velocity in the y direction is given by (B45), (B 39), (B40), summarized as

$$v = \pm \overline{Dar}(c) \text{ on } \Gamma_{13}, \text{ with } \Omega_1 \text{ in the } \pm y \text{ direction}, \tag{6.8}$$

$$v = 0 \text{ on } \Gamma_{23}, \tag{6.9}$$

$$v = -(\partial_x s)\boldsymbol{v}_0^{(1)} + \boldsymbol{v}_1^{(2)} \text{ on } \Gamma_{12}. \tag{6.10}$$

For the flow profile we solve at each x and t a cell problem for the unknown w. Summarizing (B2), (B3), (B48), (B50) and the boundary condition (5.25), the unknown w

https://doi.org/10.1017/jfm.2022.308 Published online by Cambridge University Press

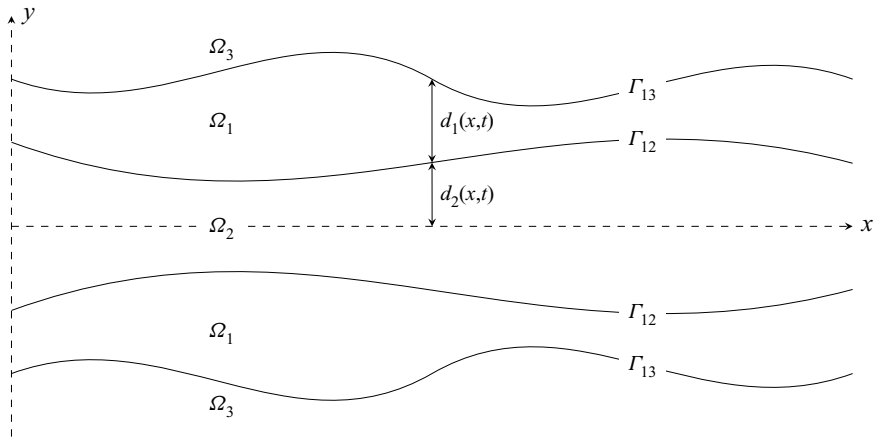

Figure 2. Symmetric geometry of two fluid phases in a thin strip.

is given by the second-order differential equation

$$-\partial_y(\gamma_1 \partial_y w) = 1 \text{ in } \Omega_1|_x, \tag{6.11}$$

$$-\partial_y(\gamma_2 \partial_y w) = 1 \text{ in } \Omega_2|_x, \tag{6.12}$$

$$\rho_3 d_0 w - \partial_y(\gamma_3 \partial_y w) = 0 \text{ in } \Omega_3|_x, \tag{6.13}$$

$$[\![w]\!] = 0 \text{ at } \Gamma_{12}, \Gamma_{13}, \Gamma_{23}, \tag{6.14}$$

$$[\![\gamma \partial_y w]\!] = 0 \text{ at } \Gamma_{12}, \Gamma_{13}, \Gamma_{23}, \tag{6.15}$$

$$w = 0 \text{ at } y = \pm \ell_\Omega/2. \tag{6.16}$$

For the transport of the fluid–fluid interface Γ_{12} in (6.10) we need the flow velocities $\boldsymbol{v}_0^{(1)}$ and $\boldsymbol{v}_1^{(2)}$. We then get the horizontal flow velocity $\boldsymbol{v}_0^{(1)}$ from (5.26), that is

$$\boldsymbol{v}_0^{(1)} = -w \partial_x p_0. \tag{6.17}$$

For the vertical flow velocity $\boldsymbol{v}_1^{(2)}$ one has to solve (B4), (B29) and (B31), summarized

$$\partial_x(\boldsymbol{v}_0^{(1)}) + \partial_y(\boldsymbol{v}_1^{(2)}) = 0 \text{ in } \Omega_1 \cup \Gamma_{12} \cup \Omega_2, \tag{6.18}$$

$$-(\partial_x s)\boldsymbol{v}_0^{(1)} + \boldsymbol{v}_1^{(2)} = 0 \text{ on } \Gamma_{13} \text{ and } \Gamma_{23}. \tag{6.19}$$

6.3. *Upscaled sharp-interface model in a simplified geometry with symmetry*

The upscaled sharp-interface model (6.1)–(6.19) uses no assumption on how the phases are distributed. When these are appearing in a fixed order, the model simplifies. In this case, there is no need to consider a general subdomain Ω_i for the phase i, it is sufficient to know the width of the phase i layer in the y direction. These widths become unknowns of the model.

We assume here the following simplified geometry. The solid phase (in Ω_3) is covered by a film of fluid 1 (occupying Ω_1). The second fluid (in Ω_2) is located in the middle of the thin strip. For simplicity, we assume symmetry around the x-axis. An illustration of the geometry is given in figure 2.

https://doi.org/10.1017/jfm.2022.308 Published online by Cambridge University Press

With functions $d_1(t,x) > 0$, $d_2(t,x) > 0$, representing the width in the y direction of the fluid phase 1, respectively 2, we can describe this situation by defining

$$\Omega_2(t) = \{(x,y) : -d_2(t,x) < y < d_2(t,x)\}, \tag{6.20}$$

$$\begin{aligned}\Omega_1(t) = {} & \{(x,y) : -d_1(t,x) - d_2(t,x) < y < -d_2(t,x)\} \\ & \cup \{(x,y) : d_2(t,x) < y < d_1(t,x) + d_2(t,x)\},\end{aligned} \tag{6.21}$$

$$\begin{aligned}\Omega_3(t) = {} & \{(x,y) : -\ell_\Omega/2 < y < -d_1(t,x) - d_2(t,x)\} \\ & \cup \{(x,y) : d_1(t,x) + d_2(t,x) < y < \ell_\Omega/2\}.\end{aligned} \tag{6.22}$$

In this geometry the solution w to the cell problem (6.11)–(6.16) depends only on the variables d_1 and d_2, and on the choice of ℓ_Ω. With a lengthy calculation we find that the terms depending on ℓ_Ω decay exponentially fast for big ℓ_Ω, and we drop them in the following. The remaining terms lead to

$$K_f = \frac{2}{\gamma_1}\left(\frac{(d_1+d_2)^3}{3} + \left(\frac{\gamma_1}{\gamma_2} - 1\right)\frac{d_2^3}{3} + L_{slip}(d_1+d_2)^2\right), \tag{6.23}$$

$$K_c = \frac{2}{\gamma_1}\left(\frac{d_1^3}{3} + \frac{d_1^2 d_2}{2} + L_{slip} d_1(d_1+d_2)\right), \tag{6.24}$$

with the slip length L_{slip} given by

$$L_{slip} = \frac{\gamma_1}{\sqrt{\rho_3 d_0 \gamma_3}}. \tag{6.25}$$

We can relate $\partial_t d_1$ and $\partial_t d_2$ with the interface velocities (6.8)–(6.10). Considering the fluid–solid interface Γ_{13} we get with (6.8)

$$\partial_t(d_1+d_2) = v = -\overline{Da}r(c), \tag{6.26}$$

while for the fluid–fluid interface Γ_{12} we calculate with (6.10), (6.18) and (6.19)

$$\begin{aligned}\partial_t d_2 &= v = -(\partial_x d_2)\boldsymbol{v}_0^{(1)}(t,x,d_2) + \boldsymbol{v}_1^{(2)}(t,x,d_2) \\ &= -(\partial_x d_2)\boldsymbol{v}_0^{(1)}(t,x,d_2) + \boldsymbol{v}_1^{(2)}(t,x,d_2) \\ &\quad + (\partial_x(d_1+d_2))\boldsymbol{v}_0^{(1)}(t,x,d_1+d_2) - \boldsymbol{v}_1^{(2)}(t,x,d_1+d_2) \\ &= (\partial_x(d_2+d_1))\boldsymbol{v}_0^{(1)}(t,x,d_1+d_2) - (\partial_x d_2)\boldsymbol{v}_0^{(1)}(t,x,d_2) - \int_{d_2}^{d_2+d_1} \partial_y \boldsymbol{v}_1^{(2)}(t,x,y)\,\mathrm{d}y \\ &= (\partial_x(d_2+d_1))\boldsymbol{v}_0^{(1)}(t,x,d_1+d_2) - (\partial_x d_2)\boldsymbol{v}_0^{(1)}(t,x,d_2) + \int_{d_2}^{d_2+d_1} \partial_x \boldsymbol{v}_0^{(1)}(t,x,y)\,\mathrm{d}y \\ &= \partial_x\left(\int_{d_2}^{d_2+d_1} \boldsymbol{v}_0^{(1)}(t,x,y)\,\mathrm{d}y\right).\end{aligned} \tag{6.27}$$

The integral equals the total fluid flux in the x direction in the upper half of Ω_1. We use (6.17), (6.6) and the symmetry of w around $y = 0$ to further calculate

$$\partial_t d_2 = \partial_x\left(\int_{d_2}^{d_2+d_1} \boldsymbol{v}_0^{(1)}\,\mathrm{d}y\right) = -\partial_x\left((\partial_x p)\int_{d_2}^{d_2+d_1} w\,\mathrm{d}y\right) = -\frac{1}{2}\partial_x\left(K_c \partial_x p\right). \tag{6.28}$$

https://doi.org/10.1017/jfm.2022.308 Published online by Cambridge University Press

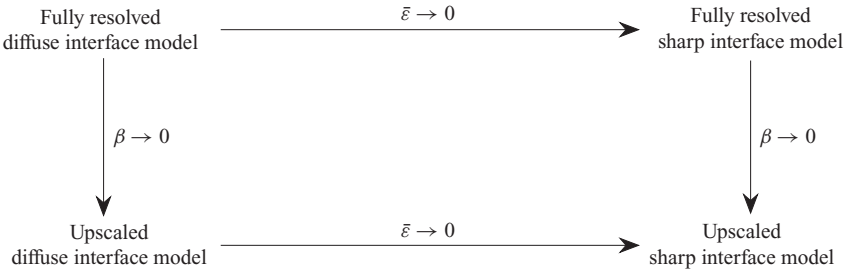

Figure 3. Models obtained by upscaling ($\beta \to 0$) and the sharp-interface limit ($\bar{\varepsilon} \to 0$).

We can now summarize (6.1), (6.2), (6.3), (6.26) and (6.26) as an upscaled model for the unknowns d_1, d_2, p, Q_f and c

$$\partial_t d_1 + \partial_t d_2 = -\overline{Da}r(c(t,x)), \tag{6.29}$$

$$\partial_t d_2 = -\frac{1}{2}\partial_x(K_c(d_1,d_2)\partial_x p), \tag{6.30}$$

$$Q_f = -K_f(d_1,d_2)\partial_x p, \tag{6.31}$$

$$\partial_x Q_f = 0, \tag{6.32}$$

$$\frac{\mathrm{d}}{\mathrm{d}t}(2d_1 c) + \partial_x((-K_c(d_1,d_2)\partial_x p)c) = \frac{1}{Pe_c}\partial_x(2d_1\partial_x c) - 2\overline{Da}r(c). \tag{6.33}$$

Remark 6.1. We can rewrite (6.30) and (6.31) to highlight the hyperbolicity of the model. As discussed in Remark 5.1 one assumption for the upscaling is that there is no occurrence of triple points. Therefore, we assume $d_1 > 0$ and $d_2 > 0$ and deduce $K_f > 0$, $K_c > 0$. We can now calculate

$$\partial_t d_2 = \frac{1}{2}Q_f\partial_x\left(\frac{K_c(d_1,d_2)}{K_f(d_1,d_2)}\right). \tag{6.34}$$

The unknown d_2 gets transported with flux $Q_f K_c/K_f$ and can show hyperbolic behaviour, such as the formation of discontinuities.

6.4. *Asymptotic consistency*

In § 5 we have investigated the limit process $\beta \to 0$, while in § 6 we examined $\bar{\varepsilon} \to 0$. A common question is under which circumstances there is asymptotic consistency, i.e. these two limit processes commute. In figure 3 all limit processes are shown in a commutative diagram.

We investigate asymptotic consistency with non-dimensional numbers chosen as in (5.5)–(5.10) with $\overline{Re}, \overline{Ca}, \overline{Da}, \bar{M}, \overline{Pe_c}$ constant and independent of $\bar{\varepsilon}$ and β. The non-dimensional δ is chosen as $\delta = \bar{\varepsilon}$.

When starting with the fully resolved diffuse-interface model (4.3)–(4.10) the limit $\bar{\varepsilon} \to 0$ results in a sharp-interface model as described in § 2. For details on this sharp-interface limit, see Rohde & von Wolff (2021).

When we assume the geometry of § 6.3 we can proceed to upscale the fully resolved sharp-interface model after introducing d_1 and d_2. While the process is tedious, the main ideas are analogous to the calculations in Sharmin *et al.* (2020). In particular, the asymptotic expansion of interface conditions, normal vectors and curvature have to be

https://doi.org/10.1017/jfm.2022.308 Published online by Cambridge University Press

handled with care, as the coordinates $\boldsymbol{x} = (x, \beta y)$ depend on β. For sake of brevity we skip this calculation here.

With the geometry of § 6.3 we find asymptotic consistency, that is the limit processes $\beta \to 0$ and $\bar{\varepsilon} \to 0$ commute. The result of the upscaling of the fully resolved sharp-interface model is exactly given by (6.29)–(6.33).

Remark 6.2. In more general geometries, asymptotic consistency does not necessary hold. This is due to the following observation. When upscaling a fully resolved diffuse-interface model, the parameter δ is constant and independent of β. This leads to $\tilde{\phi}_f > 0$ and $\tilde{\phi}_c > 0$ everywhere. Because of this, we obtain upscaled equations for p and c without further assumptions on the geometry. The upscaled variables p and c do not depend on y, even if the geometry consists of two parallel channels separated by a solid region with $\boldsymbol{\Phi} \approx \boldsymbol{e}_3$. On the other hand, when upscaling the fully resolved diffuse-interface model, the δ-modifications have already vanished, as $\delta = \bar{\varepsilon}$. In this case, it is possible to have a different pressure p in each channel, that is in each connected part of $\Omega_1|_x \cup \Omega_2|_x$. Also, it is possible to have a different ion concentration c in each connected part of $\Omega_1|_x$.

We conclude that we have asymptotic consistency under the condition that there is only one flow channel, i.e. $\Omega_1|_x \cup \Omega_2|_x$ is connected for every x, and that the first fluid phase is connected, i.e. $\Omega_1|_x$ is connected for every x. It is also possible to consider the symmetric case as in § 6.3 and have two symmetric connected parts of fluid one.

7. Numerical investigation

We will now compare the upscaled δ-2f1s-model (5.12)–(5.27) with the fully resolved δ-2f1s-model (4.3)–(4.10). Remark 6.1 suggests that shock fronts can form in the upscaled model. Note that in this case the assumptions for the upscaling in § 5 are no longer valid, and we expect different behaviours from the two models.

For the fully resolved δ-2f1s-model (4.3)–(4.10) we use a monolithic finite-element implementation provided by the DUNE-Phasefield module (von Wolff 2021). We employ Taylor–Hood elements for the flow variables velocity and pressure, and first-order Lagrange elements for the ion concentration and the phase-field parameters. The implementation is based on DUNE-PDELab (Bastian, Heimann & Marnach 2010) using ALU-Grid routines for adaptive grid generation (Alkämper *et al.* 2016).

7.1. *Numerical scheme for the upscaled δ-2f1s-model*

The upscaled δ-2f1s-model consists of multiple coupled problems. The upscaled (5.12)–(5.14) for the unknowns Q_f, p and c have parameters (5.15)–(5.18) that depend on the distribution of phases in the y-direction. This distribution is described by the fully coupled two-dimensional problem (5.19)–(5.22) for the Cahn–Hilliard variables $\phi_1, \phi_2, \phi_3, \mu_1, \mu_2, \mu_3$. Furthermore, the flow profile has to be calculated by the cell problem (5.24) and (5.25).

For simplicity, we present the numerical scheme for equidistant time steps $t_n = n\Delta t$ and equidistant discretization in x by $x_k = k\Delta x$. Let also $x_{k+1/2} = (x_k + x_{k+1})/2$. For each t_n, x_k we discretize the one-dimensional unknown $\phi^n_{1,k}(y) = \phi_1(t_n, x_k, y)$ with linear Lagrange elements, and analogously for $\phi^n_{2,k}, \phi^n_{3,k}, \mu^n_{1,k}, \mu^n_{2,k}, \mu^n_{3,k}, \boldsymbol{v}^{(1),n}_{0,k}, \boldsymbol{v}^{(2),n}_{1,k}, w^n_k$. Again, we also use this notation for other variables such as $\tilde{\phi}^n_{f,k}$.

We discretize the macroscopic unknown $c(t, x)$ with a finite volume scheme, that is $c^n(x) = c(t_n, x)$ is piecewise constant with $c(t_n, x) = c^n_k$ for $x \in (x_{k-1/2}, x_{k+1/2})$.

https://doi.org/10.1017/jfm.2022.308 Published online by Cambridge University Press

The pressure $p^n(x) = p(t_n, x)$ is discretized using linear Lagrange elements with nodes $x_{k+1/2}$. Therefore, $\partial_x p$ is constant on each finite volume cell $(x_{k-1/2}, x_{k+1/2})$.

Given $\boldsymbol{\Phi}_k^n$, c_k^n for all x_k at time t_n, we now calculate the next time step using the following algorithm.

(i) For each x_k use (5.24) and (5.25) to solve for $w_k^n(y)$. Here, we use $\boldsymbol{\Phi} = \boldsymbol{\Phi}_k^n$ and the finite element method to discretize the equation. The equations for different x_k are independent and can be solved in parallel.

(ii) For each x_k calculate $K_{f,k}^n$ and $K_{c,k}^n$ by

$$K_{f,k}^n = \int_{-\ell_\Omega/2}^{\ell_\Omega/2} \tilde{\phi}_{f,k}^n w_k^n \,\mathrm{d}y, \quad K_{c,k}^n = \int_{-\ell_\Omega/2}^{\ell_\Omega/2} \tilde{\phi}_{c,k}^n w_k^n \,\mathrm{d}y. \tag{7.1a,b}$$

(iii) Solve for $p^n(x)$ using the finite element method with

$$\partial_x(-K_f^n \partial_x p^n) = 0. \tag{7.2}$$

Here, $K_f^n(x) = K_{f,k}^n$ for $x \in (x_{k-1/2}, x_{k+1/2})$. As $K_f^n > 0$, the pressure p is either a monotonically increasing or monotonically decreasing function, depending on the boundary conditions. We assume from here on $\partial_x p^n \le 0$ and therefore fluid flow in the positive x direction. In case $\partial_x p^n \ge 0$ the upwind schemes in steps (v) and (vii) have to be modified.

(iv) For each x_k calculate $\boldsymbol{v}_{0,k}^{(1),n}(y) = -w_k^n(y)\partial_x p^n(x_k)$.

(v) Next, for each x_k we solve for $\boldsymbol{v}_{1,k}^{(2),n}$ and the Cahn–Hilliard variables $\phi_{2,k}^{n+1}, \phi_{3,k}^{n+1}, \mu_{1,k}^{n+1}, \mu_{2,k}^{n+1}, \mu_{3,k}^{n+1}$. For $\boldsymbol{v}_{1,k}^{(2),n}$ we use (5.27) the with an explicit upwind scheme for the x-derivative, i.e.

$$\partial_y(\tilde{\phi}_{f,k}^{n+1} \boldsymbol{v}_{1,k}^{(2),n}) = -\frac{\tilde{\phi}_{f,k}^n \boldsymbol{v}_{0,k}^{(1),n} - \tilde{\phi}_{f,k-1}^n \boldsymbol{v}_{0,k-1}^{(1),n}}{\Delta x}. \tag{7.3}$$

This equation is coupled with the Cahn–Hilliard cell problems (5.19)–(5.22). We again use an explicit upwinding scheme for the x-derivative, that is

$$\frac{\phi_{1,k}^{n+1} - \phi_{1,k}^n}{\Delta t} + \frac{\phi_{1,k}^n \boldsymbol{v}_{0,k}^{(1),n} - \phi_{1,k-1}^n \boldsymbol{v}_{0,k-1}^{(1),n}}{\Delta x} + \partial_y(\phi_{1,k}^{n+1} \boldsymbol{v}_{1,k}^{(2),n}) - \frac{\bar{\varepsilon}\bar{M}}{\Sigma_1}\partial_y^2 \mu_{1,k}^{n+1}$$
$$= -\frac{\overline{Da}}{\bar{\varepsilon}} q(\boldsymbol{\Phi}_k^{n+1}) \left(r(c^n(x_k)) + \tilde{\alpha}\mu_{1,k}^{n+1} - \tilde{\alpha}\mu_{3,k}^{n+1} \right), \tag{7.4}$$

$$\frac{\phi_{2,k}^{n+1} - \phi_{2,k}^n}{\Delta t} + \frac{\phi_{2,k}^n \boldsymbol{v}_{0,k}^{(1),n} - \phi_{2,k-1}^n \boldsymbol{v}_{0,k-1}^{(1),n}}{\Delta x} + \partial_y(\phi_{2,k}^{n+1} \boldsymbol{v}_{1,k}^{(2),n}) - \frac{\bar{\varepsilon}\bar{M}}{\Sigma_1}\partial_y^2 \mu_{2,k}^{n+1} = 0, \tag{7.5}$$

$$\phi_{3,k}^{n+1} = 1 - \phi_{1,k}^{n+1} - \phi_{2,k}^{n+1}, \tag{7.6}$$

$$\mu_{1,k}^{n+1} = \frac{\partial_{\phi_1} W(\boldsymbol{\Phi}_k^{n+1})}{\bar{\varepsilon}} - \bar{\varepsilon}\,\Sigma_i \partial_y^2 \phi_{1,k}^{n+1}, \tag{7.7}$$

$$\mu_{2,k}^{n+1} = \frac{\partial_{\phi_2} W(\boldsymbol{\Phi}_k^{n+1})}{\bar{\varepsilon}} - \bar{\varepsilon}\,\Sigma_i \partial_y^2 \phi_{2,k}^{n+1}, \tag{7.8}$$

$$\mu_{3,k}^{n+1} = -\mu_{1,k}^{n+1} - \mu_{2,k}^{n+1}. \tag{7.9}$$

https://doi.org/10.1017/jfm.2022.308 Published online by Cambridge University Press

Note that we do not use (5.21) and (5.22) for $\phi_{3,k}^{n+1}$ and $\mu_{3,k}^{n+1}$. Instead, we use that by construction $\phi_1 + \phi_2 + \phi_3 = 1$ and $\mu_1 + \mu_2 + \mu_3 = 0$, see (Rohde & von Wolff 2021) for details.

We use the finite element method to discretize (7.3)–(7.9) and Newtons method to solve the resulting nonlinear system. This step has by far the highest computational cost. With the explicit upwinding scheme for the x derivatives, the cell problems for each k fully decouple and can be solved in parallel. This leads to a significant speed up in comparison with discretizing the Cahn–Hilliard evolution (5.19)–(5.22) naively as a two-dimensional problem.

(vi) Calculate $\tilde{\phi}_{c,total,k}^{n+1}$ and $R_{total,k}^{n+1}$ as

$$\tilde{\phi}_{c,total,k}^{n+1} = \int_{-\ell_\Omega/2}^{\ell_\Omega/2} \phi_{c,k}^{n+1} \,\mathrm{d}y, \tag{7.10}$$

$$R_{total,k}^{n+1} = -\int_{-\ell_\Omega/2}^{\ell_\Omega/2} q(\boldsymbol{\Phi}_k^{n+1})(r(c^n(x_k)) + \tilde{\alpha}\mu_{1,k}^{n+1} - \tilde{\alpha}\mu_{3,k}^{n+1}) \,\mathrm{d}y. \tag{7.11}$$

We also set $\tilde{\phi}_{c,total,k+1/2}^{n+1} = (\tilde{\phi}_{c,total,k}^{n+1} + \tilde{\phi}_{c,total,k+1}^{n+1})/2$.

(vii) Finally we solve for c using (5.14) discretized by the finite volume method. We use an implicit upwinding scheme for the transport in the x-direction

$$\begin{aligned}&\frac{\tilde{\phi}_{c,total,k}^{n+1} c_k^{n+1} - \tilde{\phi}_{c,total,k}^{n} c_k^{n}}{\Delta t} - \frac{K_{c,k}^n \partial_x p^n(x_k) c_k^{n+1} - K_{c,k-1}^n \partial_x p^n(x_{k-1}) c_{k-1}^{n+1}}{\Delta x} \\ &\quad = \frac{1}{\overline{Pe_c}} \frac{1}{\Delta x} \left(\tilde{\phi}_{c,total,k+1/2}^{n+1} \frac{c_{k+1}^{n+1} - c_k^{n+1}}{\Delta x} - \phi_{c,total,k-1/2}^{n+1} \frac{c_k^{n+1} - c_{k-1}^{n+1}}{\Delta x} \right) + \frac{\overline{Da}}{\bar{\varepsilon}} R_{total,k}^{n+1}.\end{aligned} \tag{7.12}$$

7.2. *Comparison: formation of an N-wave*

As our first numerical example we choose a geometry as described in § 6.3, with the computational domain $(x, y) \in [0, 1] \times [-1, 0]$. For $x = 0$ and $x = 1$ we choose periodic boundary conditions for all variables except the pressure p. For $y = -1$ we use the trivially upscaled versions of the boundary conditions 5.1-5.4 and for $y = 0$ we choose boundary conditions according to the symmetry assumption.

We will compare the non-dimensional δ-2f1s-model with the upscaled δ-2f1s-model (5.12)–(5.27). For simplicity, we choose $\gamma_1 = \gamma_2$ and d_0 sufficiently big such that $L_{slip} \approx 0$. We choose the phase-field parameter $\bar{\varepsilon} = 0.03$ and $\delta = \bar{\varepsilon}$ as in § 6.

We want to focus on the hyperbolic behaviour of d_2 as described in Remark 6.1. Therefore, we choose c in the initial conditions such that $r(c) = 0$. This leads to no precipitation or dissolution in the model, and the fluid–solid interface does not change over time. We choose

$$d_1 + d_2 \equiv 0.7 \quad \text{and} \quad d_1(x) = 0.4 + 0.15 \sin(2\pi x). \tag{7.13a,b}$$

This corresponds to a plane fluid–solid interface and a sine-shaped fluid–fluid interface. An image of these initial conditions is given in figure 4.

By applying a pressure difference as Dirichlet boundary condition at $x = 0$ and $x = 1$, the two fluid phases will move in the positive x-direction. The fluid velocity $\boldsymbol{v}_0^{(1)}$ is higher in the centre of the channel. As shown in figure 4, this will lead to a steeper fluid–fluid

https://doi.org/10.1017/jfm.2022.308 Published online by Cambridge University Press

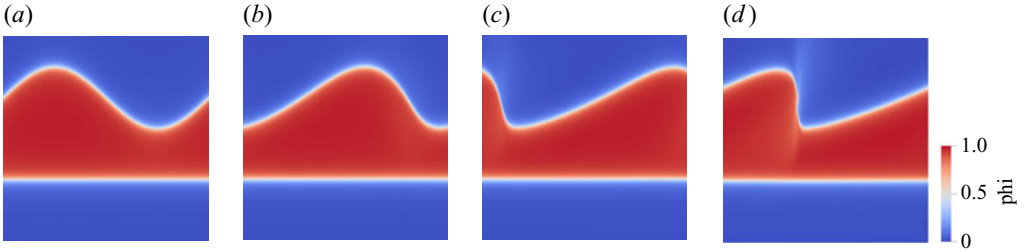

Figure 4. Evolution of the upscaled δ-$2f1s$-model on the domain $[0, 1] \times [-1, 0]$. Shown in red is fluid phase one, with fluid phase two above and solid phase below. From left to right: initial data, $t = 0.15$, $t = 0.3$ and $t = 0.45$.

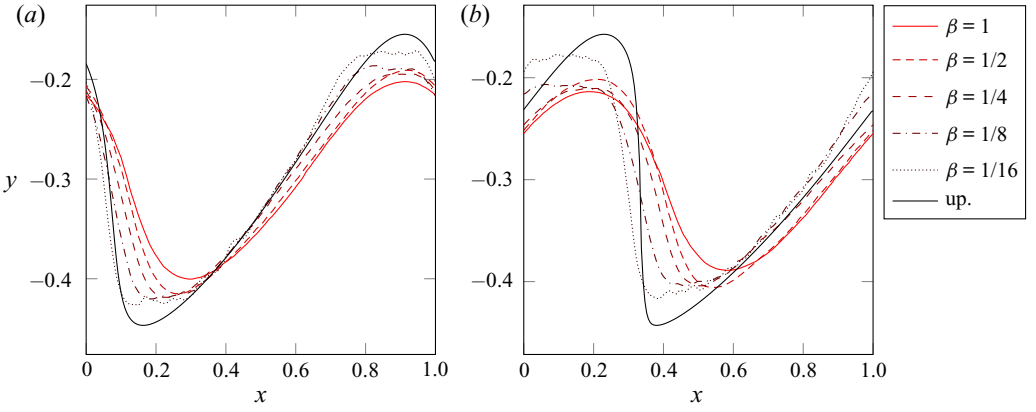

Figure 5. Fluid–fluid interface locations for the non-dimensional δ-$2f1s$-model with varying β, and for the upscaled δ-$2f1s$-model. The interface is located through the condition $\phi_1 = \phi_2$. Left: $t = 0.3$, right: $t = 0.44$.

interface over time. At a time $t^* > 0$ the upscaled δ-$2fs$-model has a fluid–fluid interface that is perpendicular to the thin strip. As discussed in Remark 5.1, the assumptions for the upscaling in § 5 are no longer valid. For times $t > t^*$ the fluid–fluid interface will roll over, leading to multiple layers of fluid phase 1 at the same x value. In § 8 we will present some ideas of how to handle such cases in future works.

We can compare this behaviour with the non-dimensional δ-$2f1s$-model in a thin strip for different values of β. As shown in figure 5, for times $t < t^*$ there is a good agreement between the non-dimensional δ-$2f1s$-model with small values of β and the upscaled δ-$2f1s$-model.

In contrast to the upscaled δ-$2f1s$-model, the non-dimensional δ-$2f1s$-model does not evolve to a fluid–fluid interface perpendicular to the thin strip, as shown in figure 5. Instead, when reaching a steep fluid–fluid interface there are regions of high curvature at the beginning and end of the steep passage. In these regions of high curvature the surface tension leads to a pressure difference between the fluid phases, counteracting the interface getting steeper. For smaller β the fluid–fluid interface allows for a steeper passage in (x, y) coordinates, as this effect depends on the curvature in the $\boldsymbol{x}$ coordinates, which are not scaled with β.

https://doi.org/10.1017/jfm.2022.308 Published online by Cambridge University Press

7.3. *Comparison: precipitation*

In the second numerical example we study precipitation in the thin strip. We use the same domain and boundary conditions as in the previous example. Again, we choose $\gamma_1 = \gamma_2$, and a d_0 large enough so that $L_{slip} \approx 0$. We further choose $\bar{\varepsilon} = 0.03$ and $\delta = \bar{\varepsilon}$. We use a simple, linear reaction rate $r(c) = c - 0.5$ and choose the ion concentration to be in equilibrium initially, that is $c = 0.5$ everywhere. With $d_1(x) = 0.4$ and $d_2(x) = 0.3$ in the initial conditions correspond to the phases being layered in the thin strip, without depending on x. To induce precipitation we add a source term $s(x)$ to the ion conservation equation (4.5), it now reads

$$\partial_t(\tilde{\phi}_c c) + \nabla \cdot (\phi_c \boldsymbol{v} c) + \frac{Cn}{\beta Pe_{CH}} \nabla \cdot (\boldsymbol{J}_1 c) = \frac{1}{Pe_c} \nabla \cdot (\tilde{\phi}_c \nabla c) + DaR + \tilde{\phi}_c s(x). \tag{7.14}$$

The source terms upscales trivially at $O(\beta^0)$, and the upscaled ion conservation equation (5.14) is now given by

$$\frac{\mathrm{d}}{\mathrm{d}t}(\tilde{\phi}_{c,total} c) + \partial_x((-K_c \partial_x p) c) = \frac{1}{\overline{Pe_c}} \partial_x(\tilde{\phi}_{c,total} \partial_x c) + \frac{\overline{Da}}{\bar{\varepsilon}} R_{total} + \tilde{\phi}_{c,total} s(x). \tag{7.15}$$

We choose the ion source to be located between $x = 0.1$ and $x = 0.3$, in detail

$$s(x) = \max(0, 62.5(x - 0.1)(0.3 - x)). \tag{7.16}$$

Figure 6 shows a comparison between the non-dimensional δ-$2f1s$-model with different values of β, and the upscaled δ-$2f1s$-model. There is a good agreement between the full model with small values of β and the upscaled model. For large values of β there is less precipitation in the thin strip. This is due to the ion concentration c not being constant in the y-direction. The source term $\tilde{\phi}_c s(x)$ generates ions everywhere in the first fluid phase, but precipitation removes ions from the first fluid phase only at the fluid–solid interface. This leads to an oversaturation $c > 0.5$ further away from the fluid–solid interface. For smaller values of β the diffusion in the y-direction results in more ions precipitating and therefore a smaller oversaturation of ions in the fluid phase.

Figure 6 also shows the influence of a non-constant width of the thin strip on the flow inside the thin strip. The fluid–fluid interfaces are pushed towards the centre of the thin strip, where flow velocities are higher.

8. Conclusion

We have upscaled a phase-field model for the incompressible flow of two immiscible fluids in the geometry of a thin strip. With the assumption of slow variation in the direction along the thin strip, we find a two-scale model as a result of the upscaling. The two-scale model consists of macroscopic equations for the total flux Q_f, the pressure p and the ion concentration c. Those equations are coupled to microscopic equations for the flow and for the geometry, represented by the phase-field variables. By discretizing the upscaled equations with a finite volume scheme, we obtain microscopic cell problems that are fully decoupled in each time step and can therefore be solved in parallel.

We have also investigated the sharp-interface limit of the upscaled phase-field model and found under additional assumptions on the geometry a fully upscaled model. This model only consists of macroscopic equations for total flux Q_f, the pressure p, the ion concentration c and the widths of each fluid phase, d_1 and d_2. Further analysis shows that the upscaling and the sharp-interface limit commute.

https://doi.org/10.1017/jfm.2022.308 Published online by Cambridge University Press

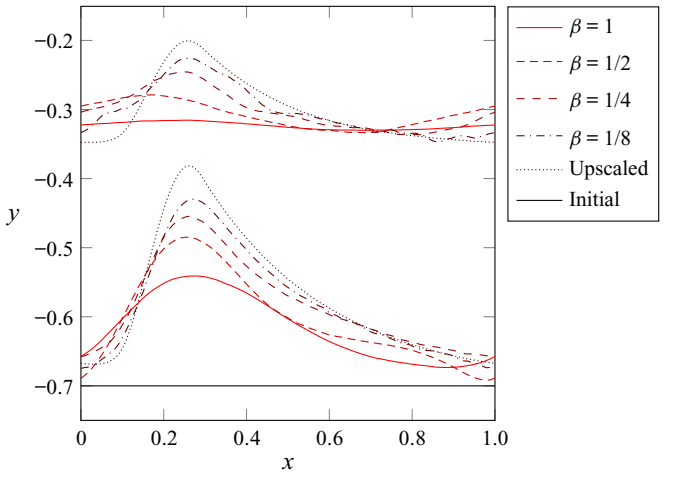

Figure 6. Interface locations at time $t = 2.4$ for the non-dimensional δ-$2f1s$-model with varying β, and for the upscaled δ-$2f1s$-model. The fluid–fluid interface can be seen in the upper half and is located by the condition $\phi_1 = \phi_2$. The fluid–solid interface in the lower half is located by $\phi_1 = \phi_3$. The initial location of the fluid–solid interface is marked by a black line.

Further research is needed to generalize this work in a multitude of directions. The most obvious next step is to consider three-dimensional geometries, such as a thin tube. In such a case, the curvature of the fluid–fluid interface will be bigger by a factor of β^{-2} compared with the two-dimensional case. With non-dimensional numbers scaling as in this work, surface tension effects will enter the leading-order equations of the momentum equation. As a result, one has to introduce a faster time scale to resolve relaxation in the cross-section towards an equilibrium state.

A second possible direction for future research is the consideration of a finite number of points where the assumption of slow variation along the thin strip is not fulfilled. This includes three-phase contact points, as well as the N waves shown in the numerical investigation. Such cases can not be upscaled with the current assumptions, and the numerical investigation shows no agreement between the fully resolved and the upscaled model. In future models it might be possible to describe regions with fast variation along the thin strip as fully resolved, and couple these regions on each side with the upscaled phase-field model.

Lastly, by increasing the complexity of the underlying phase-field model, the upscaling procedure will become increasingly difficult. Interesting effects seen in experiments include the dissolved ions being driven by electrostatic fields, as well as small mineral particles getting transported by the fluid flow.

Funding. Funded by the Deutsche Forschungsgemeinschaft (DFG, German Research Foundation) – Project Number 327154368 – SFB 1313; the Research Foundation Flanders (FWO) – Project G0G1316N; and the Hasselt University – Project BOF19BL12.

Declaration of interest. The authors report no conflict of interest.

Author ORCIDs.
Lars von Wolff https://orcid.org/0000-0003-1814-9324;
Iuliu Sorin Pop https://orcid.org/0000-0001-9647-4347.

https://doi.org/10.1017/jfm.2022.308 Published online by Cambridge University Press

Appendix A. Asymptotic expansions for the upscaling in a thin strip

In this section we will present the asymptotic expansions for the upscaling of the non-dimensional δ-2f1s-model. For all primary variables we assume the existence of asymptotic expansions of the form (5.11). In particular, we also use this notation for other variables, e.g.

$$\tilde{\phi}_f = \phi_{f,0} + \beta\phi_{f,1} + \cdots = (\phi_{1,0} + \phi_{2,0} + 2\delta\phi_{3,0}) + \beta(\phi_{1,1} + \phi_{2,1} + 2\delta\phi_{3,1}) + \cdots . \tag{A1}$$

We use Taylor expansions to handle nonlinearities, e.g.

$$r(c) = r(c_0 + \beta c_1 + \cdots) = r(c_0) + \beta r'(c_0)c_1 + O(\varepsilon^2). \tag{A2}$$

With this we can insert the asymptotic expansions into the non-dimensional δ-2f1s-model and group by powers of β. The upscaled equations will be recovered by investigating the terms with the lowest power of β.

A.1. *Expansion of the mass conservation equation* (4.3)

A.1.1. *Expansion of* (4.3), $O(\beta^{-1})$*:*
Recall that $\nabla = \boldsymbol{e}_x\partial_x + \beta^{-1}\boldsymbol{e}_y\partial_y$. Therefore, the leading-order terms of (4.3) are of $O(\beta^{-1})$, we have

$$\partial_y(\tilde{\phi}_{f,0}\boldsymbol{v}_0)\cdot\boldsymbol{e}_y = 0. \tag{A3}$$

We will denote components of $\boldsymbol{v}$ as $\boldsymbol{v}^{(1)} = \boldsymbol{v}\cdot\boldsymbol{e}_x$ and $\boldsymbol{v}^{(2)} = \boldsymbol{v}\cdot\boldsymbol{e}_y$. Note that $\tilde{\phi}_{f,0} > 0$ by construction in (3.4), so after integrating and using the leading order of boundary condition (5.4) we can divide by $\tilde{\phi}_{f,0}$ and obtain

$$\boldsymbol{v}_0^{(2)} = 0. \tag{A4}$$

As expected, there is no leading-order flow perpendicular to the thin strip.

A.1.2. *Expansion of* (4.3), $O(1)$*:*
With (A4) we get at first order

$$\partial_x(\tilde{\phi}_{f,0}\boldsymbol{v}_0^{(1)}) + \partial_y(\tilde{\phi}_{f,0}\boldsymbol{v}_1^{(2)}) = 0. \tag{A5}$$

The $O(\beta)$ term of boundary condition (5.4) reads $\boldsymbol{v}_1(y = \pm\ell_\Omega/2) = 0$. After integrating (A5) in y we can use this to get

$$\partial_x \int_{-\ell_\Omega/2}^{\ell_\Omega/2} \tilde{\phi}_{f,0}\boldsymbol{v}_0^{(1)}\,\mathrm{d}y = 0. \tag{A6}$$

Here, $\tilde{\phi}_{f,0}\boldsymbol{v}_0^{(1)}$ is the flux in the $\boldsymbol{e}_x$ direction, so (A6) implies that the total flux in the $\boldsymbol{e}_x$ direction is conserved.

A.2. *Expansion of the phase field* (4.6), (4.7), (4.8), (4.10)

A.2.1. *Expansion of* (4.10), $O(\beta^{-1})$*:*
We get with $Cn = \beta\bar{\varepsilon}$ three terms in leading order

$$\mu_{i,0} = \frac{\partial_{\phi_i} W(\boldsymbol{\Phi}_0)}{\bar{\varepsilon}} - \bar{\varepsilon}\,\Sigma_i\partial_y^2\phi_{i,0}. \tag{A7}$$

Notably from the Laplacian only derivatives in the $\boldsymbol{e}_y$-direction remain. In the upscaled model this will lead to a Cahn–Hilliard evolution that is only acting in the $\boldsymbol{e}_y$ direction.

https://doi.org/10.1017/jfm.2022.308 Published online by Cambridge University Press

A.2.2. *Expansion of* (4.6), (4.7), (4.8), $O(1)$*:*
Note that with (5.7), (5.8) and (5.9) we can write

$$\frac{Cn}{\beta Pe_{CH}} = \beta^2 \bar{\varepsilon}\bar{M} \quad \text{and} \quad Da = \frac{\overline{Da}}{\bar{\varepsilon}}. \tag{A8a,b}$$

We insert (4.9) into (4.6), (4.7), (4.8), as we do not treat $\boldsymbol{J}_i$ as a primary variable. Together with (A4) we have at leading $O(1)$

$$\partial_t \phi_{1,0} + \partial_x(\phi_{1,0}\boldsymbol{v}_0^{(1)}) + \partial_y(\phi_{1,0}\boldsymbol{v}_1^{(2)}) - \frac{\bar{\varepsilon}\bar{M}}{\Sigma_1}\partial_y^2\mu_{1,0} = \frac{\overline{Da}}{\bar{\varepsilon}}R_0, \tag{A9}$$

$$\partial_t \phi_{2,0} + \partial_x(\phi_{2,0}\boldsymbol{v}_0^{(1)}) + \partial_y(\phi_{2,0}\boldsymbol{v}_1^{(2)}) - \frac{\bar{\varepsilon}\bar{M}}{\Sigma_2}\partial_y^2\mu_{2,0} = 0, \tag{A10}$$

$$\partial_t \phi_{3,0} + \partial_x(2\delta\phi_{3,0}\boldsymbol{v}_0^{(1)}) + \partial_y(2\delta\phi_{3,0}\boldsymbol{v}_1^{(2)}) - \frac{\bar{\varepsilon}\bar{M}}{\Sigma_3}\partial_y^2\mu_{3,0} = -\frac{\overline{Da}}{\bar{\varepsilon}}R_0, \tag{A11}$$

where the leading-order term of the reaction is given by

$$R_0 = -q(\boldsymbol{\Phi}_0)(r(c_0) + \tilde{\alpha}\mu_{1,0} - \tilde{\alpha}\mu_{3,0}). \tag{A12}$$

Note that as in (A7) only the y-derivatives of the Laplacian remain at the leading order.

A.3. *Expansion of the ion conservation equation* (4.5)

A.3.1. *Expansion of* (4.5), $O(\beta^{-2})$*:*
We obtain at leading order only one $O(\beta^{-2})$ term

$$\frac{1}{\overline{Pe_c}}\partial_y(\tilde{\phi}_{c,0}\partial_y c_0) = 0. \tag{A13}$$

Integrating in y and using the leading-order term of boundary condition (5.3) results in

$$\tilde{\phi}_{c,0}\partial_y c_0 = 0. \tag{A14}$$

Because by construction $\tilde{\phi}_{c,0} > 0$, we conclude

$$\partial_y c_0 = 0. \tag{A15}$$

Therefore, c_0 is constant in the $\boldsymbol{e}_y$ direction, and we write $c_0 = c_0(t, x)$ to emphasize that c_0 only depends on the x coordinate.

A.3.2. *Expansion of* (4.5), $O(\beta^{-1})$*:*
As we found $\partial_y c_0 = 0$ in (A15), we get at first order only the term

$$\frac{1}{\overline{Pe_c}}\partial_y(\tilde{\phi}_{c,0}\partial_y c_1) = 0. \tag{A16}$$

With analogous argumentation to the $O(\beta^{-2})$ case we get $\partial_y c_1 = 0$ and can write $c_1 = c_1(t, x)$ to show that c_1 is independent of y.

https://doi.org/10.1017/jfm.2022.308 Published online by Cambridge University Press

A.3.3. *Expansion of* (4.5), $O(1)$*:*
Similar to the $O(1)$ expansion of (4.6), (4.7) and (4.8), we insert the Cahn–Hilliard flux $\boldsymbol{J}_i$ (4.9) and the non-dimensional numbers (A8*a*,*b*) into the equation, and use (A4). We obtain the second-order terms

$$\partial_t(\tilde{\phi}_{c,0}c_0) + \partial_x(\phi_{c,0}\boldsymbol{v}_0^{(1)}c_0) + \partial_y(\phi_{c,0}\boldsymbol{v}_1^{(2)}c_0) - \frac{\bar{\varepsilon}\bar{M}}{\Sigma_1}\partial_y(c_0\partial_y\mu_{1,0})$$
$$= \frac{1}{\overline{Pe_c}}\partial_x(\tilde{\phi}_{c,0}\partial_x c_0) + \frac{1}{Pe_c}\partial_y(\tilde{\phi}_{c,0}\partial_y c_2) + \frac{\overline{Da}}{\bar{\varepsilon}}R_0, \tag{A17}$$

where R_0 is given by (A12). After integrating in y we can use the boundary conditions (5.2), (5.3) and (5.4) to eliminate the terms containing a y derivative. We obtain

$$\frac{\mathrm{d}}{\mathrm{d}t}\left(c_0\int_{-\ell_\Omega/2}^{\ell_\Omega/2}\tilde{\phi}_{c,0}\,\mathrm{d}y\right) + \partial_x\left(c_0\int_{-\ell_\Omega/2}^{\ell_\Omega/2}\phi_{c,0}\boldsymbol{v}_0^{(1)}\,\mathrm{d}y\right)$$
$$= \frac{1}{\overline{Pe_c}}\partial_x\left(\left(\int_{-\ell_\Omega/2}^{\ell_\Omega/2}\tilde{\phi}_{c,0}\,\mathrm{d}y\right)\partial_x c_0\right) + \frac{\overline{Da}}{\bar{\varepsilon}}\int_{-\ell_\Omega/2}^{\ell_\Omega/2}R_0\,\mathrm{d}y. \tag{A18}$$

Here, we have written c_0 outside the integrals to emphasize that c_0 does not depend on y. Equation (A18) is a transport–diffusion–reaction equation for $c_0(x,t)$, where the coefficients still depend on the exact distribution of $\boldsymbol{\Phi}_0$ in the $\boldsymbol{e}_y$ direction.

A.4. *Expansion of the momentum equation* (4.6)

A.4.1. *Expansion of* (4.4), $O(\beta^{-3})$*:*
The only term of $O(\beta^{-3})$ is

$$-\frac{1}{\overline{Re}}\tilde{\phi}_{f,0}\boldsymbol{e}_y\partial_y p_0 = 0. \tag{A19}$$

As $\tilde{\phi}_{f,0}$ is positive by construction, we conclude that p_0 does not depend on y and write $p_0 = p_0(t,x)$.

A.4.2. *Expansion of* (4.4)$\cdot\boldsymbol{e}_x$, $O(\beta^{-2})$*:*
We investigate at the first order only the equation for the x-component. With (A4) and $p_0 = p_0(t,x)$ the remaining terms are

$$-\frac{1}{\overline{Re}}\tilde{\phi}_{f,0}\partial_x p_0 + \frac{1}{\overline{Re}}\partial_y(\tilde{\gamma}(\boldsymbol{\Phi}_0)\partial_y\boldsymbol{v}_0^{(1)}) - \frac{1}{\overline{Re}}\rho_3 d(\tilde{\phi}_{f,0})\boldsymbol{v}_0^{(1)} = 0. \tag{A20}$$

We can interpret this as a linear differential equation for $\boldsymbol{v}_0^{(1)}$ with boundary conditions (5.4). In particular, we can use the linearity to write

$$\boldsymbol{v}_0^{(1)}(t,x,y) = -w(t,x,y)\partial_x p_0(t,x), \tag{A21}$$

where w is the solution to the cell problem

$$\rho_3 d(\tilde{\phi}_{f,0})w - \partial_y(\tilde{\gamma}(\boldsymbol{\Phi}_0)\partial_y w) = \tilde{\phi}_{f,0}, \tag{A22}$$
$$w(t,x,\pm\ell_\Omega/2) = 0. \tag{A23}$$

For a given $\boldsymbol{\Phi}$ the function w calculates the parabolic flow profile in the cross-section of the thin strip. As we expect from a Darcy-type flow, the fluid velocity is proportional to $-\partial_x p_0$, shown in (A21).

https://doi.org/10.1017/jfm.2022.308 Published online by Cambridge University Press

Remark A.1. We note that by construction $\tilde{\gamma} > 0$ and therefore the cell problem (A22), (A23) has a unique solution.

Appendix B. Matched asymptotic expansions for the sharp-interface limit of the upscaled δ-2f1s-model

In this section we present the sharp-interface limit of the upscaled δ-2f1s-model under the assumptions made in § 6.1. The sharp interface limit consists of asymptotic expansions in the bulk phases (outer expansions), asymptotic expansions in the interface regions (inner expansions) and the matching of these asymptotic expansions.

B.1. *Outer expansions*

For the bulk phases we assume that we can write solutions to the upscaled δ-2f1s-model (5.12)–(5.27) in terms of an outer asymptotic expansion in $\bar{\varepsilon}$ for the variables $\boldsymbol{\Phi}, w, \boldsymbol{v}_0^{(1)}, \boldsymbol{v}_1^{(2)}, p, c, \mu_1, \mu_2, \mu_3$. That is, similar to the expansions in § 5.2, we assume expansions of the form

$$\boldsymbol{\Phi}(t,x,y) = \boldsymbol{\Phi}_0^{out}(t,x,y) + \bar{\varepsilon}\boldsymbol{\Phi}_1^{out}(t,x,y) + \bar{\varepsilon}^2\boldsymbol{\Phi}_2^{out}(t,x,y) + \cdots . \tag{B1}$$

Here, the outer expansion terms $\boldsymbol{\Phi}_k^{out}$, $k \in \mathbb{N}_0$ are independent of $\bar{\varepsilon}$. The expansions for the macroscopic variables $p(x)$, $c(x)$ do not depend on y. We will insert these expansions into the upscaled δ-2f1s-model and group by orders of $\bar{\varepsilon}$. Analogously to Appendix A we handle nonlinearities by Taylor expansion.

B.1.1. *Outer expansion of* (5.22)*, $O(\beta^{-1})$:*

We can argue as in Rohde & von Wolff (2021) to find that the only stable solutions to the leading-order terms are $\boldsymbol{\Phi}_0^{out} = \boldsymbol{e}_k$, $k \in \{1,2,3\}$ with the restriction $\phi_{k,1}^{out} \leq 0$ and $\phi_{i,1}^{out}, \phi_{j,1}^{out} \geq 0$ for $\{i,j\} = \{1,2,3\} \setminus \{k\}$. The additional restriction stems from the fact that the triple-well potential W depends on $\delta = \bar{\varepsilon}$.

We define the set $\Omega_k(t)$ to be the set of (x,y) where $\boldsymbol{\Phi}_0^{out}(t,x,y) = \boldsymbol{e}_k$. In the sharp-interface formulation $\Omega_k(t)$ will represent the domain of phase k.

B.1.2. *Outer expansion of* (5.24)*, $O(1)$:*

In Ω_3, i.e. in case $\boldsymbol{\Phi}_0^{out} = \boldsymbol{e}_3$, we have $\tilde{\phi}_{f,0}^{out} = 0$ and the leading order reads

$$\rho_3 d_0 w_0^{out} - \partial_y(\gamma_3 \partial_y w_0^{out}) = 0, \tag{B2}$$

where $d_0 = d(0) > 0$. In the fluid phases Ω_i, $i \in \{1,2\}$, we have $\boldsymbol{\Phi}_0^{out} = \boldsymbol{e}_i$ and therefore $\tilde{\phi}_{f,0}^{out} = 1$. Note that by construction $d(1) = 0$. With this we obtain at leading order

$$-\partial_y(\gamma_i \partial_y w_0^{out}) = 1. \tag{B3}$$

B.1.3. *Outer expansion of* (5.27)*, $O(1)$:*

In the fluid phases $\boldsymbol{\Phi}_0^{out} = \boldsymbol{e}_i$, $i \in \{1,2\}$ we have $\tilde{\phi}_{f,0}^{out} = 1$ and obtain

$$\partial_x(\boldsymbol{v}_{0,0}^{(1),out}) + \partial_y(\boldsymbol{v}_{1,0}^{(2),out}) = 0. \tag{B4}$$

https://doi.org/10.1017/jfm.2022.308 Published online by Cambridge University Press

B.1.4. *Outer expansion of* (5.12), (5.13), $O(1)$*:*
We now consider the macroscopic equations. The equations for the flow (5.12), (5.13) upscale trivially, the leading order reads

$$\partial_x Q_{f,0}^{out} = 0, \tag{B5}$$

$$Q_{f,0}^{out} = -K_{f,0}^{out} \partial_x p_0^{out}, \tag{B6}$$

where the parameter $K_{f,0}^{out}$ is the leading-order expansion of K_f, using (5.16)

$$K_{f,0}^{out} = \int_{-\ell_\Omega/2}^{\ell_\Omega/2} \phi_{f,0}^{out} w_{f,0}^{out} \,\mathrm{d}y. \tag{B7}$$

Note that the leading-order expansion of $\tilde{\phi}_f$ is $\phi_{f,0}^{out}$ as the δ-modification is of $O(\bar{\varepsilon})$ because of the scaling choice $\delta = \bar{\varepsilon}$.

B.1.5. *Outer expansion of* (5.14), $O(1)$*:*
For the transport–diffusion–reaction equation for c let us first investigate the reaction term. We have with (5.18) and (5.23)

$$\frac{\overline{Da}}{\bar{\varepsilon}} R_{total} = -\frac{\overline{Da}}{\bar{\varepsilon}} \int_{-\ell_\Omega/2}^{\ell_\Omega/2} q(\boldsymbol{\Phi})(r(c) + \tilde{\alpha}\mu_1 - \tilde{\alpha}\mu_3) \,\mathrm{d}y. \tag{B8}$$

As $q(\boldsymbol{\Phi}^{out}) = O(\varepsilon^2)$ in the bulk phases $\boldsymbol{\phi}_0^{out} = \boldsymbol{e}_k$, $k \in \{1, 2, 3\}$, there is no contribution of the reaction term in the bulk at leading order. Note that there will be a contribution of this term in the interface regions, see § B.2. Overall we have for (5.14) at leading order

$$\frac{\mathrm{d}}{\mathrm{d}t}(\phi_{c,total,0}^{out} c_0^{out}) + \partial_x((-K_{c,0}^{out} \partial_x p_0^{out}) c_0^{out}) = \frac{1}{\overline{Pe_c}} \partial_x(\phi_{c,total,0}^{out} \partial_x c_0^{out}) + \overline{Da} R_{interface,0}, \tag{B9}$$

with coefficients

$$\phi_{c,total,0}^{out} = \int_{-\ell_\Omega/2}^{\ell_\Omega/2} \phi_{c,0}^{out} \,\mathrm{d}y, \tag{B10}$$

$$K_{c,0}^{out} = \int_{-\ell_\Omega/2}^{\ell_\Omega/2} \phi_{c,0}^{out} w_{f,0}^{out} \,\mathrm{d}y, \tag{B11}$$

and $R_{interface,0}$ as a placeholder for the interface contributions of the reaction term.

B.2. *Inner expansions*

We have shown in § B.1 that the domain is partitioned into Ω_1, Ω_2 and Ω_3. We locate the interfaces between the phases as

$$\Gamma_{ij}(t) = \{(x, y) \in \Omega : \phi_i(t, x, y) = \phi_j(t, x, y) \geq 1/3\}. \tag{B12}$$

We assume that Γ_{ij} is a smooth, one-dimensional manifold. As explained in Remark 5.1 we do not consider triple points, where all three phases meet, and do not allow for the interfaces to touch the boundary of Ω at $y = \pm\ell_\Omega/2$. Also, interfaces cannot occur perpendicular to the thin strip and therefore there exists locally around an interface Γ_{ij} a unique mapping $s(t, x)$ such that $(x, s(t, x)) \in \Gamma_{ij}$.

https://doi.org/10.1017/jfm.2022.308 Published online by Cambridge University Press

We use this mapping to introduce a new coordinate z close to the interface

$$z(x,t) = \frac{y - s(t,x)}{\bar{\varepsilon}}. \tag{B13}$$

Because we expect the interface width to be of size $\bar{\varepsilon}$, the coordinate z is scaled by ε^{-1}. The velocity of Γ_{ij} at (x,s) in the y-direction is given by

$$v(x) = \partial_t s(t,x). \tag{B14}$$

We will use the new coordinates (t,x,z) as the coordinates to describe the interfaces Γ_{ij}. For a generic function $f(t,x,y) = f^{in}(t,x,z)$ we obtain the transformation rules

$$\partial_t f = -\frac{1}{\varepsilon} v \partial_z f^{in} + \partial_t f^{in}, \tag{B15}$$

$$\partial_y f = \frac{1}{\varepsilon} \partial_z f^{in}, \tag{B16}$$

$$\partial_x f = -\frac{1}{\varepsilon} (\partial_x s) \partial_z f^{in} + \partial_x f^{in}. \tag{B17}$$

We assume that, close to an interface Γ_{ij}, we can write solutions to the upscaled δ-$2f1s$-model (5.12)–(5.27) in terms of an inner asymptotic expansion in $\bar{\varepsilon}$ for the variables $\boldsymbol{\Phi}$, w, $\boldsymbol{v}_0^{(1)}$, $\boldsymbol{v}_1^{(2)}$, μ_1, μ_2, μ_3. That is we assume expansions of the form

$$\boldsymbol{\Phi}(t,x,y) = \boldsymbol{\Phi}_0^{in}(t,x,z) + \bar{\varepsilon} \boldsymbol{\Phi}_1^{in}(t,x,z) + \bar{\varepsilon}^2 \boldsymbol{\Phi}_2^{in}(t,x,z) + \cdots, \tag{B18}$$

with coefficients $\boldsymbol{\Phi}_k^{in}$ independent of $\bar{\varepsilon}$. In contrast to the outer asymptotic expansions, the inner asymptotic expansions depend on the (t,x,z) coordinates. This will lead to different terms being of the highest order when inserting the expansions into the upscaled δ-$2f1s$-model. We do not use inner expansions of the macroscopic variables p and c, as they are constant across all interfaces.

To relate inner and outer expansions, we match the limit value of inner expansions for $z \to \pm\infty$ with the limit value of the outer expansions at s (from the respective side). The matching conditions are well studied (Caginalp & Fife 1988), we use

$$\lim_{z\to\pm\infty} \boldsymbol{\Phi}_0^{in}(t,x,z) = \lim_{y\to 0^+} \boldsymbol{\Phi}_0^{out}(t,x,s\pm y), \tag{B19}$$

$$\lim_{z\to\pm\infty} \partial_z \boldsymbol{\Phi}_0^{in}(t,x,z) = 0, \tag{B20}$$

$$\lim_{z\to\pm\infty} \partial_z \boldsymbol{\Phi}_1^{in}(t,x,z) = \lim_{y\to 0^+} \partial_y \boldsymbol{\Phi}_0^{out}(t,x,s\pm y). \tag{B21}$$

B.2.1. *Inner expansion of* (5.22)*,* $O(\bar{\varepsilon}^{-1})$*:*
Consider an interface between bulk phases $\boldsymbol{\Phi}_0^{out} = \boldsymbol{e}_i$ and $\boldsymbol{\Phi}_0^{out} = \boldsymbol{e}_j$. With matching condition (B19) this means

$$\lim_{z\to-\infty} \boldsymbol{\Phi}_0^{in} = \boldsymbol{e}_i \quad \text{and} \quad \lim_{z\to\infty} \boldsymbol{\Phi}_0^{in} = \boldsymbol{e}_j. \tag{B22a,b}$$

Then by assumption we have no third phase contributions across the interface, that is

$$\phi_{k,0}^{in} = 0, \quad \text{with } k \in \{1,2,3\} \setminus \{i,j\}. \tag{B23}$$

https://doi.org/10.1017/jfm.2022.308 Published online by Cambridge University Press

Following the argument in Rohde & von Wolff (2021) we calculate the leading-order terms of (5.22) for μ_k and find $\phi_{j,0}^{in}$ as a solution to the ordinary differential equation

$$W'_{dw}(\phi_{j,0}^{in}) - \partial_z^2 \phi_{j,0}^{in} = 0, \tag{B24}$$

with additional conditions

$$\lim_{z\to-\infty} \phi_{j,0}^{in} = 0, \quad \lim_{z\to-\infty} \phi_{j,0}^{in} = 1, \quad \phi_{j,0}^{in}(t, x, 0) = 1/2. \tag{B25}$$

The first two conditions are boundary conditions from (B22*a*,*b*) while the third condition stems from definition of Γ_{ij} (B12) and centres the interface at $z = 0$. With a lengthy calculation $\phi_{j,0}^{in}$ is implicitly given by

$$z = \frac{1}{30}\left(\frac{1}{1-\phi_{j,0}^{in}} - \frac{1}{\phi_{j,0}^{in}} + 2\log\left(\frac{\phi_{j,0}^{in}}{1-\phi_{j,0}^{in}}\right)\right). \tag{B26}$$

We find $\phi_{i,0}^{in}$ by $\phi_{i,0}^{in} = 1 - \phi_{j,0}^{in}$.

B.2.2. *Inner expansion of* (5.27)*,* $O(\bar{\varepsilon}^{-1})$*:*
Using the coordinate transformations (B16) and (B17), we get at leading order

$$-(\partial_x s)\partial_z(\phi_{f,0}^{in}\boldsymbol{v}_{0,0}^{(1),in}) + \partial_z(\phi_{f,0}^{in}\boldsymbol{v}_{1,0}^{(2),in}) = 0. \tag{B27}$$

Note that $\partial_x s(t, x)$ does not depend on z and therefore

$$-(\partial_x s)\phi_{f,0}^{in}\boldsymbol{v}_{0,0}^{(1),in} + \phi_{f,0}^{in}\boldsymbol{v}_{1,0}^{(2),in} = \text{const.}, \tag{B28}$$

with respect to z. Across the interface Γ_{12} we have $\phi_{f,0}^{in} = 1$ and thus with matching condition (B19) we get for all $z \in \mathbb{R}$

$$\begin{aligned}
&-(\partial_x s)\boldsymbol{v}_{0,0}^{(1),in}(t, x, z) + \boldsymbol{v}_{1,0}^{(2),in}(t, x, z)\\
&\quad= \lim_{z\to\pm\infty} -(\partial_x s)\boldsymbol{v}_{0,0}^{(1),in}(t, x, z) + \boldsymbol{v}_{1,0}^{(2),in}(t, x, z)\\
&\quad= \lim_{y\to 0^+} -(\partial_x s)\boldsymbol{v}_{0,0}^{(1),out}(t, x, s \pm y) + \boldsymbol{v}_{1,0}^{(2),out}(t, x, s \pm y).
\end{aligned} \tag{B29}$$

In particular, this means that the term $-(\partial_x s)\boldsymbol{v}_{0,0}^{(1),out} + \boldsymbol{v}_{1,0}^{(2),out}$ is continuous across the Γ_{12} interface.

When matching (B28) at the fluid–solid interfaces Γ_{13} and Γ_{23}, $\phi_{f,0}^{in}$ vanishes in the limit towards the solid phase, we can conclude

$$-(\partial_x s)\phi_{f,0}^{in}\boldsymbol{v}_{0,0}^{(1),in} + \phi_{f,0}^{in}\boldsymbol{v}_{1,0}^{(2),in} = 0. \tag{B30}$$

Using matching condition (B19) we find

$$-(\partial_x s)\boldsymbol{v}_{0,0}^{(1),out} + \boldsymbol{v}_{1,0}^{(2),out} = 0, \tag{B31}$$

for the fluid velocity. This condition therefore allows only for fluid flow parallel to the fluid–solid interfaces.

https://doi.org/10.1017/jfm.2022.308 Published online by Cambridge University Press

B.2.3. *Inner expansion of* (5.19), (5.20), (5.21), $O(\bar{\varepsilon}^{-1})$*:*
We will argue analogously to Rohde & von Wolff (2021). The leading-order expansions for (5.19), (5.20) and (5.21) are given by

$$\begin{aligned} &-\nu\partial_z\phi_{1,0}^{in} - (\partial_x s)\partial_z(\phi_{1,0}^{in}\boldsymbol{v}_{0,0}^{(1),in}) + \partial_z(\phi_{1,0}^{in}\boldsymbol{v}_{1,0}^{(2),in}) - \frac{\bar{M}}{\Sigma_1}\partial_z^2\mu_{1,0}^{in} \\ &\quad = -\overline{Da}q(\boldsymbol{\Phi}_0^{in})(r(c_0^{out}) + \alpha\mu_{1,0}^{in} - \alpha\mu_{3,0}^{in}), \end{aligned} \tag{B32}$$

$$-\nu\partial_z\phi_{2,0}^{in} - (\partial_x s)\partial_z(\phi_{2,0}^{in}\boldsymbol{v}_{0,0}^{(1),in}) + \partial_z(\phi_{2,0}^{in}\boldsymbol{v}_{1,0}^{(2),in}) - \frac{\bar{M}}{\Sigma_2}\partial_z^2\mu_{2,0}^{in} = 0, \tag{B33}$$

$$-\nu\partial_z\phi_{3,0}^{in} - \frac{\bar{M}}{\Sigma_3}\partial_z^2\mu_{3,0}^{in} = +\overline{Da}\, q(\boldsymbol{\Phi}_0^{in})(r(c_0^{out}) + \alpha\mu_{1,0}^{in} - \alpha\mu_{3,0}^{in}). \tag{B34}$$

Let us first consider the interface Γ_{13}, with Ω_1 being in the negative z direction. Here $\phi_{1,0}^{in} = \phi_{f,0}^{in}$ and with (B30) the advection terms vanish from (B32). We also have no third phase contributions and therefore $\phi_{1,0}^{in} + \phi_{3,0}^{in} = 1$. With notation $\mu_{3-1} := \mu_{3,0}^{in} - \mu_{1,0}^{in}$ we calculate $\Sigma_3\cdot$ (B34) $-\Sigma_1\cdot$ (B32)

$$-(\Sigma_1+\Sigma_3)\nu\partial_z\phi_{3,0}^{in} - \bar{M}\partial_z^2\mu_{3-1} = (\Sigma_1+\Sigma_3)\overline{Da}q(\boldsymbol{\Phi}_0^{in})(r(c_0^{out}) - \alpha\mu_{3-1}). \tag{B35}$$

In Rohde & von Wolff (2021) it is shown that with (B24) and by construction of q the identity $q(\boldsymbol{\Phi}_0^{in}) = \partial_z\phi_{3,0}^{in}$ holds. We can interpret (B35) as an ordinary differential equation for μ_{3-1} with boundary conditions $\lim_{z\to\pm\infty}\partial_z\mu_{3-1} = 0$ (by using matching condition (B20)).

In the case $\alpha = 0$ all constant functions μ_{3-1} are solutions to the differential equation, under the compatibility condition

$$\nu = -\overline{Da}r(c_0^{out}). \tag{B36}$$

In case $\alpha > 0$ the unique solution to (B35) is given by the constant function

$$\mu_{3-1} = \alpha^{-1}(\nu + \overline{Da}\, r(c_0^{out})). \tag{B37}$$

We can combine (B36) and (B37), and also consider the case that the fluid and solid side of the Γ_{13} interface is switched. Overall we conclude

$$\nu = \begin{cases} \alpha(\mu_{1,0}^{in} - \mu_{3,0}^{in}) + \overline{Da}r(c) & \text{if } \lim_{z\to-\infty}\boldsymbol{\Phi}_0^{in} = \boldsymbol{e}_3 \text{ and } \lim_{z\to\infty}\boldsymbol{\Phi}_0^{in} = \boldsymbol{e}_1, \\ \alpha(\mu_{3,0}^{in} - \mu_{1,0}^{in}) - \overline{Da}r(c) & \text{if } \lim_{z\to-\infty}\boldsymbol{\Phi}_0^{in} = \boldsymbol{e}_1 \text{ and } \lim_{z\to\infty}\boldsymbol{\Phi}_0^{in} = \boldsymbol{e}_3. \end{cases} \tag{B38}$$

For Γ_{23} we can argue analogously to the Γ_{13} case. Because there is no precipitation, i.e. $q(\boldsymbol{\Phi}_0^{in}) = 0$, we obtain

$$\mu_{3,0}^{in} - \mu_{2,0}^{in} = \text{const.} \quad \text{and} \quad \nu = 0. \tag{B39a,b}$$

Lastly, we consider the fluid–fluid interface Γ_{12}, with Ω_1 in the direction of negative z. There is no precipitation process, so with $q(\boldsymbol{\Phi}_0^{in}) = 0$ we integrate over (B32) and use matching conditions (B19) for $\phi_{1,0}^{in}$ and (B20) for $\partial_z\mu_{1,0}^{in}$ and obtain

$$\nu = -(\partial_x s)\boldsymbol{v}_{0,0}^{(1),in} + \boldsymbol{v}_{1,0}^{(2),in}. \tag{B40}$$

Furthermore $\mu_{1,0}^{in}$ has to be constant in z, and with an analogous argument using (B33) also $\mu_{2,0}^{in}$ is constant.

https://doi.org/10.1017/jfm.2022.308 Published online by Cambridge University Press

B.2.4. *Inner expansion of* (5.22)*,* $O(1)$*:*
We consider the interface Γ_{ij} with Ω_i in the negative z direction. We assume the absence of a third phase, that is $\phi^{in}_{k,0} = 0$, $k \in \{1, 2, 3\} \setminus \{i, j\}$, and find by construction of W in (3.2) that $\partial_{\phi_i} W'(\boldsymbol{\Phi}^{in}_0) = W'_{dw}(\phi^{in}_{i,0})$. We examine the difference $\mu_i - \mu_j$ at first order and find

$$\mu^{in}_{i,0} - \mu^{in}_{j,0} = \Sigma_i W''_{dw}(\phi^{in}_{i,0})\phi^{in}_{i,1} - \Sigma_i \partial_z^2 \phi^{in}_{i,1} - \Sigma_j W''_{dw}(\phi^{in}_{j,0})\phi^{in}_{j,1} + \Sigma_j \partial_z^2 \phi^{in}_{j,1}. \tag{B41}$$

In the absence of a third phase $\phi^{in}_{i,0} + \phi^{in}_{j,0} = 1$, and by construction $W_{dw}(\phi)$ is symmetric around $\phi = 1/2$. Therefore, $W''_{dw}(\phi^{in}_{i,0}) = W''_{dw}(\phi^{in}_{j,0})$, and we rewrite (B41) as

$$\mu^{in}_{i,0} - \mu^{in}_{j,0} = (W''_{dw}(\phi^{in}_{j,0}) - \partial_z^2)(\Sigma_i \phi^{in}_{i,1} - \Sigma_j \phi^{in}_{j,1}). \tag{B42}$$

Recall that $\mu^{in}_{i,0} - \mu^{in}_{j,0}$ is constant across the interface Γ_{ij}. After multiplying with $\partial_z \phi^{in}_{j,0}$ and integrating over z we calculate

$$\begin{aligned}
\mu^{in}_{i,0} - \mu^{in}_{j,0} &= \int_{-\infty}^{\infty} (\partial_z \phi^{in}_{j,0})(\mu^{in}_{i,0} - \mu^{in}_{j,0})\,\mathrm{d}z \\
&= \int_{-\infty}^{\infty} (\partial_z \phi^{in}_{j,0})(W''_{dw}(\phi^{in}_{j,0}) - \partial_z^2)(\Sigma_i \phi^{in}_{i,1} - \Sigma_j \phi^{in}_{j,1})\,\mathrm{d}z \\
&= \int_{-\infty}^{\infty} (W''_{dw}(\phi^{in}_{j,0})\partial_z \phi^{in}_{j,0} - \partial_z^3 \phi^{in}_{j,0})(\Sigma_i \phi^{in}_{i,1} - \Sigma_j \phi^{in}_{j,1})\,\mathrm{d}z \\
&= \int_{-\infty}^{\infty} \partial_z (W'_{dw}(\phi^{in}_{j,0}) - \partial_z^2 \phi^{in}_{j,0})(\Sigma_i \phi^{in}_{i,1} - \Sigma_j \phi^{in}_{j,1})\,\mathrm{d}z \\
&= 0.
\end{aligned} \tag{B43}$$

We have used partial integration to get to the third line, the boundary terms vanish with matching condition (B21) and the structure of $\phi^{in}_{j,0}$ (B26). The fourth line evaluates to zero with the identity (B24). Note that, compared with Rohde & von Wolff (2021), there is no curvature term in this calculation, as the Cahn–Hilliard evolution acts only in the y-direction.

We conclude

$$\mu^{in}_{i,0} = \mu^{in}_{j,0}. \tag{B44}$$

and (B38) simplifies to

$$v = \begin{cases} +\overline{Dar}(c) & \text{if } \lim_{z\to-\infty} \boldsymbol{\Phi}^{in}_0 = \boldsymbol{e}_3 \text{ and } \lim_{z\to\infty} \boldsymbol{\Phi}^{in}_0 = \boldsymbol{e}_1, \\ -\overline{Dar}(c) & \text{if } \lim_{z\to-\infty} \boldsymbol{\Phi}^{in}_0 = \boldsymbol{e}_1 \text{ and } \lim_{z\to\infty} \boldsymbol{\Phi}^{in}_0 = \boldsymbol{e}_3. \end{cases} \tag{B45}$$

B.2.5. *Inner expansion of* (5.24)*,* $O(\bar{\varepsilon}^{-2})$*:*
At leading order the equation reads

$$\partial_z(\gamma(\boldsymbol{\Phi}^{in}_0)\partial_z w^{in}_0) = 0. \tag{B46}$$

After integrating in y we use matching condition (B20) divide by $\gamma(\boldsymbol{\Phi}^{in}_0) > 0$ and find

$$\partial_z w^{in}_0 = 0, \tag{B47}$$

that is w is constant across the interface. With matching condition (B20) this implies

$$\lim_{y\to 0^+} w^{out}_0(t, x, s + y) = \lim_{y\to 0^+} w^{out}_0(t, x, s - y). \tag{B48}$$

https://doi.org/10.1017/jfm.2022.308 Published online by Cambridge University Press

B.2.6. *Inner expansion of* (5.24)*,* $O(\bar{\varepsilon}^{-1})$*:*
With (B47) the first-order term of (5.24) reads

$$\partial_z(\gamma(\boldsymbol{\Phi}_0^{in})\partial_z w_1^{in}) = 0. \tag{B49}$$

We integrate and with matching conditions (B19), (B21) we get

$$\lim_{y\to 0^+}(\gamma(\boldsymbol{\Phi}_0^{out}(t,x,s+y)\partial_y w_0^{out}(t,x,s+y)) = \lim_{y\to 0^+}(\gamma(\boldsymbol{\Phi}_0^{out}(t,x,s-y)\partial_y w_0^{out}(t,x,s-y)). \tag{B50}$$

B.2.7. *Inner expansion of* (5.14)*,* $O(1)$*:*
We only need to investigate the reaction term

$$\frac{\overline{Da}}{\bar{\varepsilon}}R_{total} = -\frac{\overline{Da}}{\bar{\varepsilon}}\int_{-\ell_\Omega/2}^{\ell_\Omega/2} q(\boldsymbol{\Phi})(r(c)+\tilde{\alpha}\mu_1-\tilde{\alpha}\mu_3)\,\mathrm{d}y. \tag{B51}$$

On Γ_{12} and Γ_{23} we have $q(\boldsymbol{\Phi}^{in}) = O(\bar{\varepsilon}^2)$ and therefore no leading-order contribution. Let us consider Γ_{13} with Ω_1 in the negative z direction. Using (B44) the leading-order term of the integrand is $q(\boldsymbol{\Phi}_0^{in})r(c_0^{out})$. Transforming the integral to the z coordinate results in the leading-order term of $O(1)$

$$-\overline{Da}r(c_0^{out})\int_{-\infty}^{\infty} q(\boldsymbol{\Phi}_0^{in})\,\mathrm{d}z. \tag{B52}$$

In Rohde & von Wolff (2021) it is shown that by construction of q we have $q(\boldsymbol{\Phi}_0^{in}) = \mathrm{d}_z\phi_{3,0}^{in}$. With matching condition (B19) the integral evaluates to one. When considering Γ_{13} with Ω_1 in the positive z direction we get the same result.

There might be multiple Γ_{13} interfaces contributing to the macroscopic reaction term. Therefore, the total contribution to (5.14) at $O(1)$ is

$$\overline{Da}R_{interface} = -\overline{Da}N(\Gamma_{13})r(c_0^{out}), \tag{B53}$$

with $N(\Gamma_{13})$ being the number of Γ_{13} interfaces for a fixed x.

References

Abels, H., Garcke, H. & Grün, G. 2012 Thermodynamically consistent, frame indifferent diffuse interface models for incompressible two-phase flows with different densities. *Math. Models Meth. Appl. Sci.* **22** (03), 1150013.

Agosti, A., Giovanardi, B., Formaggia, L. & Scotti, A. 2016 A numerical procedure for geochemical compaction in the presence of discontinuous reactions. *Adv. Water Resour.* **94**, 332–344.

Alkämper, M., Dedner, A., Klöfkorn, R. & Nolte, M. 2016 The DUNE-ALUGrid module. *Arch. Numer. Softw.* **4** (1), 1–28.

Allen, S.M. & Cahn, J.W. 1979 A microscopic theory for antiphase boundary motion and its application to antiphase domain coarsening. *Acta Metall.* **27** (6), 1085–1095.

Bahar, T., Golfier, F., Oltean, C. & Benioug, M. 2016 An upscaled model for bio-enhanced NAPL dissolution in porous media. *Transp. Porous Med.* **113**, 653–693.

Baňas, L. & Mahato, H.S. 2017 Homogenization of evolutionary Stokes–Cahn–Hilliard equations for two-phase porous media flow. *Asymptot. Anal.* **105**, 77–95.

Bastian, P., Heimann, F. & Marnach, S. 2010 Generic implementation of finite element methods in the distributed and unified numerics environment (dune). *Kybernetika* **2**, 294–315

https://doi.org/10.1017/jfm.2022.308 Published online by Cambridge University Press

BECKERMANN, C., DIEPERS, H.-J., STEINBACH, I., KARMA, A. & TONG, X. 1999 Modeling melt convection in phase-field simulations of solidification. *J. Comput. Phys.* **154** (2), 468–496.

BOYER, F. & LAPUERTA, C. 2006 Study of a three component Cahn–Hilliard flow model. *Math. Model. Anal.* **40**, 653–687.

BOYER, F., LAPUERTA, C., MINJEAUD, S., PIAR, B. & QUINTARD, M. 2010 Cahn–Hilliard/Navier–Stokes model for the simulation of three-phase flows. *Transp. Porous Med.* **82** (3), 463–483.

BOYER, F. & MINJEAUD, S. 2014 Hierarchy of consistent n-component Cahn–Hilliard systems. *Math. Models Meth. Appl. Sci.* **24** (14), 2885–2928.

BRINGEDAL, C., BERRE, I., POP, I.S. & RADU, F.A. 2015 Pore scale model for non-isothermal flow and mineral precipitation and dissolution in a thin strip. *J. Comput. Appl. Maths* **289**, 346–355.

BRINGEDAL, C., BERRE, I., POP, I.S. & RADU, F.A. 2016 Upscaling of non-isothermal reactive porous media flow with changing porosity. *Transp. Porous Med.* **114**, 371–393.

BRINGEDAL, C., VON WOLFF, L. & POP, I.S. 2020 Phase field modeling of precipitation and dissolution processes in porous media: upscaling and numerical experiments. *Multiscale Model. Simul.* **18** (2), 1076–1112.

BUNOIU, R., CARDONE, G., KENGNE, R. & WOUKENG, J.L. 2020 Homogenization of 2D Cahn–Hilliard-Navier–Stokes system. *J. Elliptic Parabol. Equ.* **6**, 377–408.

CAGINALP, G. & FIFE, P.C. 1988 Dynamics of layered interfaces arising from phase boundaries. *SIAM J. Appl. Maths* **48** (3), 506–518.

CAHN, J.W. & HILLIARD, J.E. 1958 Free energy of a nonuniform system. I. Interfacial free energy. *J. Chem. Phys.* **28** (2), 258–267.

DALY, K.R. & ROOSE, T. 2015 Homogenization of two fluid flow in porous media. *Proc. R. Soc.* A *Math. Phys. Engng Sci.* **471**, 20140564.

DENTZ, M., LE BORGNE, T., ENGLERT, A. & BIJELJIC, B. 2011 Mixing, spreading and reaction in heterogeneous media: a brief review. *J. Contam. Hydrol.* **120-121**, 1–17.

VAN DUIJN, C.J. & KNABNER, P. 1997 Travelling wave behaviour of crystal dissolution in porous media flow. *Eur. J. Appl. Maths* **8**, 49–92.

DUNBAR, O., LAM, K.F. & STINNER, B. 2019 Phase field modelling of surfactants in multi-phase flow. *Interfaces Free Bound.* **21**, 495–547.

GRAY, W.G. & MILLER, C.T. 2005 Thermodynamically constrained averaging theory approach for modeling flow and transport phenomena in porous medium systems: 1. Motivation and overview. *Adv. Water Resour.* **28**, 161–180.

JACKSON, A.S., RYBAK, I., HELMIG, R., GRAY, W.G. & MILLER, C.T. 2012 Thermodynamically constrained averaging theory approach for modeling flow and transport phenomena in porous medium systems: 9. Transition region models. *Adv. Water Resour.* **42**, 71–90.

KUMAR, K., VAN NOORDEN, T.L. & POP, I.S. 2011 Effective dispersion equations for reactive flows involving free boundaries at the micro-scale. *Multiscale Model. Simul.* **9** (1), 29–58.

KUMAR, K., WHEELER, M.F. & WICK, T. 2013 Reactive flow and reaction-induced boundary movement in a thin channel. *SIAM J. Sci. Comput.* **35**, B1235–B1266.

LUNOWA, S.B., BRINGEDAL, C. & POP, I.S. 2021 On an averaged model for immiscible two-phase flow with surface tension and dynamic contact angle in a thin strip. *Stud. Appl. Maths* **147**, 84–126.

METZGER, S. & KNABNER, P. 2021 Homogenization of two-phase flow in porous media from pore to Darcy scale: a phase-field approach. *Multiscale Model. Simul.* **19**, 320–343.

MIKELIĆ, A. 2009 On an averaged model for the 2-fluid immiscible flow with surface tension in a thin cylindrical tube. *Comput. Geosci.* **7**, 183–196.

MIKELIĆ, A. & PAOLI, L. 2000 On the derivation of the Buckley–Leverett model from the two fluid Navier–Stokes equations in a thin domain. *Comput. Geosci.* **4** (1), 99–101.

NAVIER, C.L.M.H. 1823 Mémoire sur les lois du mouvement des fluides. *Mém. Acad. R. Sci. Inst. France* **6** (1823), 389–440.

VAN NOORDEN, T.L. 2009*a* Crystal precipitation and dissolution in a thin strip. *Eur. J. Appl. Maths* **20**, 69–91.

VAN NOORDEN, T.L. 2009*b* Crystal precipitation and dissolution in a porous medium: effective equations and numerical experiments. *Multiscale Model. Simul.* **7**, 1220–1236.

VAN NOORDEN, T.L. & ECK, C. 2011 Phase field approximation of a kinetic moving-boundary problem modelling dissolution and precipitation. *Interfaces Free Bound.* **13** (1), 29–55.

PEGO, R.L. & PENROSE, O. 1989 Front migration in the nonlinear Cahn–Hilliard equation. *Proc. R. Soc. Lond.* A*: Math. Phys. Sci.* **422** (1863), 261–278.

PICCHI, D. & BATTIATO, I. 2018 The impact of pore-scale flow regimes on upscaling of immiscible two-phase flow in porous media. *Water Resour. Res.* **54**, 6683–6707.

https://doi.org/10.1017/jfm.2022.308 Published online by Cambridge University Press

QUINTARD, M. & WHITAKER, S. 1988 Two-phase flow in heterogeneous porous media: the method of large-scale averaging. *Transp. Porous Med.* **3**, 357–413.

QUINTARD, M. & WHITAKER, S. 1994 Convection, dispersion, and interfacial transport of contaminants: homogeneous porous media. *Adv. Water Resour.* **17**, 221–239.

REDEKER, M., ROHDE, C. & SORIN POP, I. 2016 Upscaling of a tri-phase phase-field model for precipitation in porous media. *IMA J. Appl. Maths* **81** (5), 898–939.

ROHDE, C. & VON WOLFF, L. 2021 A ternary Cahn–Hilliard–Navier–Stokes model for two-phase flow with precipitation and dissolution. *Math. Models Meth. Appl. Sci.* **31** (1), 1–35.

RYBAK, I.V., GRAY, W.G. & MILLER, C.T. 2015 Modeling two-fluid-phase flow and species transport in porous media. *J. Hydrol.* **521**, 565–581.

SCHMUCK, M., PRADAS, M., PAVLIOTIS, G.A. & KALLIADASIS, S. 2012 Upscaled phase-field models for interfacial dynamics in strongly heterogeneous domains. *Proc. R. Soc.* A *Math. Phys. Engng Sci.* **468**, 3705–3724.

SCHMUCK, M., PRADAS, M., PAVLIOTIS, G.A. & KALLIADASIS, S. 2013 Derivation of effective macroscopic Stokes–Cahn–Hilliard equations for periodic immiscible flows in porous media. *Nonlinearity* **26**, 3259–3277.

SCHULZ, R. 2019 Crystal precipitation and dissolution in a porous medium: evolving microstructure and perforated solid matrix. *Spec. Topic Rev. Porous Media* **10**, 305–321.

SCHULZ, R., RAY, N., FRANK, F., MAHATO, H.S. & KNABNER, P. 2017 Strong solvability up to clogging of an effective diffusion-precipitation model in an evolving porous medium. *Eur. J. Appl. Maths* **28**, 179–207.

SHARMIN, S., BRINGEDAL, C. & POP, I.S. 2020 On upscaling pore-scale models for two-phase flow with evolving interfaces. *Adv. Water Res.* **142**, 103646.

SUN, Y. & BECKERMANN, C. 2004 Diffuse interface modeling of two-phase flows based on averaging: mass and momentum equations. *Phys.* D **198** (3), 281–308.

TARTAKOVSKY, A.M., MEAKIN, P., SCHEIBE, T.D. & WOOD, B.D. 2007 A smoothed particle hydrodynamics model for reactive transport and mineral precipitation in porous and fractured porous media. *Water Resour. Res.* **43** (5). Available at: https://agupubs.onlinelibrary.wiley.com/doi/pdf/10.1029/2005WR004770.

WHITAKER, S. 1986 Flow in porous media II: the governing equations for immiscible, two-phase flow. *Transp. Porous Med.* **1**, 105–125.

VON WOLFF, L. 2021 The DUNE-phasefield module (release 1.0).

VON WOLFF, L., WEINHARDT, F., CLASS, H., HOMMEL, J. & ROHDE, C. 2021 Investigation of crystal growth in enzymatically induced calcite precipitation by micro-fluidic experimental methods and comparison with mathematical modeling. *Transp. Porous Med.* **137** (2), 327–343.

https://doi.org/10.1017/jfm.2022.308 Published online by Cambridge University Press